

SN 2020jgb: A Peculiar Type Ia Supernova Triggered by a Massive Helium-Shell Detonation in a Star-Forming Galaxy

CHANG LIU,¹ ADAM A. MILLER,¹ ABIGAIL POLIN,^{2,3} ANYA E. NUGENT,¹ KISHALAY DE,^{4,*} PETER E. NUGENT,^{5,6} STEVE SCHULZE,⁷ AVISHAY GAL-YAM,⁸ CHRISTOFFER FREMLING,^{9,10} SHREYA ANAND,¹¹ IGOR ANDREONI,^{12,13,14,†} PETER BLANCHARD,¹ THOMAS G. BRINK,¹⁵ SUHAIL DHAWAN,¹⁶ ALEXEI V. FILIPPENKO,¹⁵ KATE MAGUIRE,¹⁷ TASSILO SCHWEYER,¹⁸ HUEI SEARS,¹ YASHVI SHARMA,¹⁰ MATTHEW J. GRAHAM,¹⁰ STEVEN L. GROOM,¹⁹ DAVID HALE,⁹ MANSI M. KASLIWAL,¹⁰ SHRINIVAS R. KULKARNI,¹⁰ FRANK J. MASCI,¹⁹ JOSIAH PURDUM,⁹ BENJAMIN RACINE,²⁰ AND JESPER SOLLERMAN¹⁸

¹Center for Interdisciplinary Exploration and Research in Astrophysics (CIERA), Department of Physics and Astronomy, Northwestern University, 1800 Sherman Road, Evanston, IL 60201, USA

²The Observatories of the Carnegie Institution for Science, 813 Santa Barbara Street, Pasadena, CA 91101, USA

³TAPIR, Walter Burke Institute for Theoretical Physics, 350-17, Caltech, Pasadena, CA 91125, USA

⁴MIT-Kavli Institute for Astrophysics and Space Research, 77 Massachusetts Ave., Cambridge, MA 02139, USA

⁵Department of Astronomy, University of California, Berkeley, CA 94720, USA

⁶Lawrence Berkeley National Laboratory, 1 Cyclotron Road, Berkeley, CA, 94720, USA

⁷The Oskar Klein Centre, Department of Physics, Stockholm University, AlbaNova University Center, SE 106 91 Stockholm, Sweden

⁸Department of particle physics and astrophysics, Weizmann Institute of Science, 76100 Rehovot, Israel

⁹Caltech Optical Observatories, California Institute of Technology, Pasadena, CA 91125, USA

¹⁰Division of Physics, Mathematics, and Astronomy, California Institute of Technology, Pasadena, CA 91125, USA

¹¹Cahill Center for Astrophysics, California Institute of Technology, Pasadena CA 91125, USA

¹²Joint Space-Science Institute, University of Maryland, College Park, MD 20742, USA.

¹³Department of Astronomy, University of Maryland, College Park, MD 20742, USA.

¹⁴Astrophysics Science Division, NASA Goddard Space Flight Center, Mail Code 661, Greenbelt, MD 20771, USA

¹⁵Department of Astronomy, University of California, Berkeley, CA 94720-3411, USA

¹⁶Institute of Astronomy and Kavli Institute for Cosmology, University of Cambridge, Madingley Road, Cambridge CB3 0HA, UK

¹⁷School of Physics, Trinity College Dublin, The University of Dublin, Dublin 2, Ireland

¹⁸The Oskar Klein Centre, Department of Astronomy, Stockholm University, AlbaNova, SE-106 91 Stockholm, Sweden

¹⁹IPAC, California Institute of Technology, 1200 E. California Blvd, Pasadena, CA 91125, USA

²⁰Aix Marseille Univ, CNRS/IN2P3, CPPM, Marseille, France

ABSTRACT

The detonation of a thin ($\lesssim 0.03 M_{\odot}$) helium shell (He-shell) atop a $\sim 1 M_{\odot}$ white dwarf (WD) is a promising mechanism to explain normal Type Ia supernovae (SNe Ia), while thicker He-shells and less massive WDs may explain some recently observed peculiar SNe Ia. We present observations of SN 2020jgb, a peculiar SNIa discovered by the Zwicky Transient Facility (ZTF). Near maximum light, SN 2020jgb is slightly subluminous (ZTF g -band absolute magnitude M_g between -18.2 and -18.7 mag depending on the amount of host galaxy extinction) and shows an unusually red color ($g_{\text{ZTF}} - r_{\text{ZTF}}$ between 0.4 and 0.2 mag) due to strong line-blanketing blueward of $\sim 5000 \text{ \AA}$. These properties resemble those of SN 2018byg, a peculiar SNIa consistent with a thick He-shell double detonation (DDet) SN. Using detailed radiative transfer models, we show that the optical spectroscopic and photometric evolution of SN 2020jgb are broadly consistent with a $\sim 0.95 M_{\odot}$ (C/O core + He-shell; up to $\sim 1.00 M_{\odot}$ depending on the total host extinction) progenitor ignited by a thick ($\sim 0.13 M_{\odot}$) He-shell. We detect a prominent absorption feature at $\sim 1 \mu\text{m}$ in the near-infrared (NIR) spectrum of SN 2020jgb, which could originate from unburnt helium in the outermost ejecta. While the sample size is limited, similar $1 \mu\text{m}$ features have been detected in all the thick He-shell DDet candidates with NIR spectra obtained to date. SN 2020jgb is also the first subluminous, thick He-shell DDet SN discovered in a star-forming galaxy, indisputably showing that He-shell DDet objects occur in both star-forming and passive galaxies, consistent with the normal SNIa population.

Keywords: Supernovae (1668), Type Ia supernovae (1728), White dwarf stars (1799), Observational astronomy (1145), Surveys (1671)

1. INTRODUCTION

It has been clear for decades that Type Ia supernovae (SNe Ia) are caused by the thermonuclear explosions of carbon-oxygen (C/O) white dwarfs (WDs) in binary systems (see Maoz et al. 2014, for a review). Nevertheless, the nature of the binary companion, as well as how it ignites the WD, remains highly uncertain.

The helium-shell (He-shell) double detonation (DDet) scenario is one of the most promising channels to produce SNe Ia. In this scenario, the WD accretes from a companion to develop a helium-rich shell, which, after becoming sufficiently massive, could detonate. Such a detonation sends a shock wave into the C/O core to trigger a runaway thermonuclear explosion that inevitably disrupts and destroys the entire WD (Nomoto 1982a,b; Woosley et al. 1986; Livne 1990; Woosley & Weaver 1994; Livne & Arnett 1995). This DDet mechanism can produce explosions of WDs below the Chandrasekhar-mass (M_{Ch}).

There are several observational benchmarks for He-shell DDet SNe. Shortly after the ignition of the He-shell, the decay of radioactive material in the helium ashes may power a detectable flash (Woosley & Weaver 1994; Fink et al. 2010; Kromer et al. 2010). The Fe-group elements in the ashes will blanket blue photons with wavelengths $\lesssim 5000 \text{ \AA}$ (Kromer et al. 2010), the duration of which depends on the mass of the He-shell. For shells that are sufficiently thick, Boyle et al. (2017) suggest that the unburnt helium could provide an observational signal in near-infrared (NIR) spectra, and for those with a low progenitor mass ($\lesssim 1.0 M_{\odot}$), Polin et al. (2021) predict significant [Ca II] emission in the nebular phase of the SNe.

The He-shell DDet scenario could naturally account for the observational diversity in the SNe Ia population. Using different sets of He-shell mass and C/O core mass, one can reproduce a variety of observables in “normal” SNe Ia with typical luminosities and spectral features near peak light (e.g., Polin et al. 2019; Townsley et al. 2019; Shen et al. 2021), or peculiar subluminal ones (e.g., Polin et al. 2019).

For the He-shell DDet SNe that show “normal” characteristics near peak brightness, the mass of the C/O core should be $\gtrsim 1 M_{\odot}$, and the mass of the He-shell is

expected to be low ($\lesssim 0.03 M_{\odot}$; Polin et al. 2019; Magee et al. 2021; Shen et al. 2021). Recently, it was reported that SN 2018aoz (Ni et al. 2022a), an SNe Ia showing a rapid redward color evolution within ~ 12 hr after first light, could be explained by a sub- M_{Ch} DDet model (a $1.05 M_{\odot}$ C/O core and a $0.03 M_{\odot}$ He-shell). After this red excess, the photometric evolution is consistent with that of normal SNe Ia, when the ashes of the thin He-shell become optically thin. However, some of its properties at maximum-light and in the nebular phase are not consistent with a He-shell DDet scenario (Ni et al. 2022b), making its nature debatable. To date, only a small fraction of SNe Ia have been discovered sufficiently early for possible detection of early flashes (e.g., Deckers et al. 2022). While there could be a large underlying population of normal SNe Ia triggered by He-shell DDet, currently it is hard to verify this scenario.

In contrast, if the He-shell is sufficiently massive, such that the ashes of the shell remain optically thick over a much more extended time, the SN could appear unusually red even near maximum light. Such peculiar SNe Ia could be normal in brightness, SN 2016jhr being the only reported event that shows a normal peak brightness ($M_B \approx -18.8$ mag), but exhibits an early red flash and maintains a red $g - r$ color throughout its evolution (Jiang et al. 2017). Its photometric evolution as well as around-maximum spectrum could be explained by a near- M_{Ch} DDet model. WD explosions with a total progenitor mass $< 1 M_{\odot}$ are expected to be subluminal. SN 2018byg (De et al. 2019) is a prototype of this subclass. During the late stages of preparing this paper, Dong et al. (2022a) presented another thick He-shell DDet candidate, SN 2016dsg, accompanied with an archival transient OGLE-2013-SN-079 (Inserra et al. 2015). All three events are faint, red, and show strong line-blanketing in maximum-light spectra. A tentative detection of unburnt helium in SN 2016dsg was also reported by Dong et al. (2022a). We refer to these peculiar events as thick He-shell DDet SNe, which best characterize the physics leading to their peculiarities, with the caveat that the threshold of a He-shell being “thick” depends on the core mass. The small sample size to date suggests that thick He-shell events might be intrinsically rare.

It has been proposed that some, if not all, of the calcium-rich (Ca-rich) gap transients, a population of faint SNe with conspicuous [Ca II] emission in the nebular phase (Filippenko et al. 2003; Perets et al.

* NASA Einstein Fellow

† Neil Gehrels Fellow

2010; Kasliwal et al. 2012), also arise from He-shell DDet (Dessart & Hillier 2015; De et al. 2020; Polin et al. 2021). A subclass of Ca-rich transients resemble SNe Ia near peak light (termed Ca-Ia objects), marked by strong Si II absorption and the absence of optical He I lines. There are only three Ca-Ia objects (PTF 09dav, SN 2016hmk, and SN 2019ofm; De et al. 2020), all showing mild to strong line-blanketing in spectra, and hence could be He-shell DDet objects (e.g., Jacobson-Galán et al. 2020). Nonetheless, they also exhibit properties similar to those of other types of subluminal SNe Ia, such as the strong O I absorption widely seen in SN 1991bg-like (91bg-like; Filippenko et al. 1992) objects but not prominent in other He-shell DDet candidates. PTF 09dav shows the weakest line-blanketing among the three and exhibits features that are attributed to some rare elements such as Sc II (Sullivan et al. 2011), which cannot be immediately explained by either He-shell DDet or deflagration models. SN 2016hmk could also be explained by the deflagration of a near- M_{Ch} WD (Galbany et al. 2019). In summary, the nature of Ca-Ia objects remains ambiguous.

In this paper, we present observations of another thick He-shell DDet event, SN 2020jgb. This peculiar SN Ia highly resembles SN 2018byg in photometric and spectroscopic properties, and exhibits a remarkable feature in the NIR spectrum that could be attributed to unburnt helium. In Section 2, we report the observations of SN 2020jgb, which are analyzed in Section 3, where we show its similarities with other He-shell DDet SNe and discuss the tentative He I absorption features. We use a grid of He-shell DDet models to fit the data of SN 2020jgb, and present the results in Section 4.1. Then we expand our discussion to other He-shell DDet SNe, discussing the possibly ubiquitous absorption features in their NIR spectra near $1\mu\text{m}$ (Section 4.2) and their diversity in host environments (Section 4.3). We draw our conclusions in Section 5.

Along with this paper, we have released the data utilized in this study and the software used for data analysis and visualization. They are available online at <https://github.com/slowdivePTG/SN2020jgb>.

2. OBSERVATIONS

2.1. Discovery

SN 2020jgb was first discovered by the Zwicky Transient Facility (ZTF; Bellm et al. 2019a; Graham et al. 2019; Dekany et al. 2020) on 2020 May 03.463 (UT dates are used throughout this paper; MJD 58972.463) with the 48-inch Samuel Oschin Telescope (P48) at Palomar Observatory. The automated ZTF discovery pipeline (Masci et al. 2019) detected SN 2020jgb using the image-

differencing technique of Zackay et al. (2016). The candidate passed internal thresholds (e.g., Mahabal et al. 2019; Duev et al. 2019), leading to the production and dissemination of a real-time alert (Patterson et al. 2019) and the internal designation ZTF20aayhacx. It was detected with $g_{\text{ZTF}} = 19.86 \pm 0.15\text{ mag}$ at $\alpha_{\text{J2000}} = 17^{\text{h}}53^{\text{m}}12^{\text{s}}.651$, $\delta_{\text{J2000}} = -00^{\circ}51'21''81$ and announced to the public by Fremling (2020). The host galaxy, PSO J175312.663+005122.078, is a dwarf galaxy, to which SN 2020jgb has a projected offset of only $0''.3$. The last nondetection limits the brightness to $r_{\text{ZTF}} > 20.7\text{ mag}$ on 2020 April 27.477 (MJD 58966.477; 5.99 days before the first detection). This transient was classified as an SN Ia by Dahiwalé & Fremling (2020). We confirm this classification via SuperNova IDentification (SNID; Blondin & Tonry 2007), which shows SN 2020jgb is most consistent with SNe Ia. Templates of other hydrogen-poor SNe, including Type Ib and Type Ic SNe, do not match the spectra of SN 2020jgb.

2.2. Host Galaxy Observations

On 2022 March 31, two years after the transient faded, we took a spectrum of its host galaxy using the DEep Imaging Multi-Object Spectrograph (DEIMOS; Faber et al. 2003) on the Keck-II 10 m telescope, with a total integration time of 3200 s. It was reduced with the PyPeIt Python package (Prochaska et al. 2020). The host exhibits strong, narrow emission lines including $\text{H}\alpha$, $\text{H}\beta$, $[\text{N II}] \lambda\lambda 6548, 6583$, $[\text{O III}] \lambda\lambda 4959, 5007$, and $[\text{S II}] \lambda\lambda 6716, 6731$. By fitting all these emission features with Gaussian profiles, we obtain an average redshift of $z = 0.0309 \pm 0.0003$. With the diagnostic emission line equivalent width (EW) ratios ($\log [\text{N II}]/\text{H}\alpha = -1.05 \pm 0.08$ and $\log [\text{O III}]/\text{H}\beta = 0.19 \pm 0.02$)¹, the host is consistent with star-forming galaxies in the Baldwin et al. (1981, hereafter BPT) diagram (see also Veilleux & Osterbrock 1987). Additional discussion of the host galaxy properties is presented in Section 4.3.

To estimate the distance modulus of SN 2020jgb, we first use the 2M++ model (Carrick et al. 2015) to estimate the peculiar velocity of its host galaxy, PSO J175312.663+005122.078, to be $179 \pm 250\text{ km s}^{-1}$. This, combined with the recession velocity in the frame of the cosmic microwave background² (CMB) $v_{\text{CMB}} = 9136\text{ km s}^{-1}$, yields a net Hubble recession velocity of $9307 \pm 250\text{ km s}^{-1}$. Adopting $H_0 = 70\text{ km s}^{-1}\text{ Mpc}^{-1}$, $\Omega_M = 0.3$, and $\Omega_\Lambda = 0.7$, we estimate the luminosity

¹ Here $[\text{N II}]$ denotes the EW of the $[\text{N II}] \lambda 6583$ line, and $[\text{O III}]$ denotes the EW of the $[\text{O III}] \lambda 5007$ line.

² https://ned.ipac.caltech.edu/velocity_calculator

distance of SN 2020jgb to be 136.1 Mpc, equivalent to a distance modulus of $\mu = 35.67 \pm 0.06$ mag.

To evaluate the potential host galaxy extinction, we measure the Balmer decrement and find the flux ratio of $H\alpha$ to $H\beta$ to be 3.26 ± 0.13 , while the theoretical, extinction-free value is 2.86 (assuming case B recombination; Osterbrock & Ferland 2006). Using the extinction law from Fitzpatrick (1999) and assuming $R_V = 3.1$, this yields $E(B - V) = 0.11 \pm 0.04$ mag. This result is consistent with a model of the host galaxy spectral energy distribution (SED; illustrated in Section 4.3), $E(B - V) = 0.13 \pm 0.01$ mag. As we do not know the precise location of SN 2020jgb within its host galaxy, we adopt these reddening values as an upper limit to the total host-galaxy reddening.

2.3. Optical Photometry

SN 2020jgb was monitored in the g_{ZTF} and r_{ZTF} bands by ZTF as part of its ongoing Northern Sky Survey (Bellm et al. 2019b). We adopt a Galactic extinction of $E(B - V)_{MW} = 0.404$ mag (Schlafly & Finkbeiner 2011), and correct all photometry using the Fitzpatrick (1999) extinction model. The host extinction is not well constrained. While the potential host extinction could be up to $E(B - V)_{host} \approx 0.13$, the lack of Na I D absorption at the redshift of the host galaxy is consistent with no additional host extinction, though see Poznanski et al. (2011) for caveats on the use of Na I D absorption as a proxy for extinction. Thus throughout the paper, we adopt a fiducial assumption of no host extinction and discuss the possible effects of additional extinction on constraining the progenitor properties in Section 4.1. Unless otherwise specified, the data displayed in the figures are only corrected for Galactic extinction.

The forced-photometry absolute light curves³ in g_{ZTF} and r_{ZTF} are shown in Figure 1, where we display all measurements having a signal-to-noise ratio (SNR) greater than 2. The light curves are reduced using the pipeline from Miller et al. (2022, in preparation); see also Yao et al. (2019).

2.4. Optical Spectroscopy

We obtained optical spectra of the object from ~ -10 d to $\sim +150$ d relative to the r_{ZTF} -band peak, using the Spectral Energy Distribution Machine (SEDm; Blagorodnova et al. 2018) on the automated 60 inch telescope (P60; Cenko et al. 2006) at Palomar Observatory, the Kast Double Spectrograph (Miller & Stone 1994) on the Shane 3 m telescope at Lick Observatory, the Andalucia Faint Object Spectrograph and Camera

Table 1. Spectroscopic observations of SN 2020jgb and the host galaxy.

| t_{obs} | Phase | Telescope/ | R | Range | Airmass |
|------------------|--------|----------------|-----------------------------|------------------|---------|
| (MJD) | (d) | Instrument | ($\lambda/\Delta\lambda$) | (\AA) | |
| 58,976.42 | −9.7 | P60/SEDm | 100 | 3770–9220 | 1.23 |
| 58,982.12 | −4.2 | NOT/ALFOSC | 360 | 4000–9620 | 1.17 |
| 58,990.43 | +3.9 | P60/SEDm | 100 | 3770–9220 | 1.23 |
| 58,997.44 | +10.7 | P60/SEDm | 100 | 3770–9220 | 1.29 |
| 58,998.41 | +11.6 | Shane/Kast | 750 | 3620–10720 | 1.28 |
| 59,008.41 | +21.3 | P60/SEDm | 100 | 3770–9220 | 1.28 |
| 59,009.45 | +22.4 | Gemini-N/GNIRS | 1800 | 8230–25150 | 1.07 |
| 59,010.40 | +23.3 | P200/DBSP | 700 | 3200–9500 | 1.27 |
| 59,023.58 | +36.1 | Keck I/LRIS | 1100 | 3200–10250 | 2.04 |
| 59,107.29 | +117.3 | Keck I/LRIS | 1100 | 3200–10250 | 1.31 |
| 59,143.26 | +152.2 | Keck I/LRIS | 1100 | 3200–10250 | 2.16 |
| 59,669.60 | host | Keck II/DEIMOS | 2100 | 4500–8700 | 1.14 |

NOTE—Phase is measured relative to the r_{ZTF} -band peak in the host galaxy rest frame. The resolution R is reported for the central region of the spectrum.

(ALFOSC)⁴ installed at the Nordic Optical Telescope (NOT), the Double Beam Spectrograph (DBSP) on the 200 inch Hale telescope (P200; Oke & Gunn 1982), and the Low Resolution Imaging Spectrometer (LRIS) on the Keck-I 10 m telescope (Oke et al. 1995). With the exception of observations obtained with SEDm, all spectra were reduced using standard procedures (e.g., Matheson et al. 2000). The SEDm spectra were reduced using the custom `pysedm` software package (Rigault et al. 2019). Details of the spectroscopic observations are listed in Table 1, and the resulting spectral sequence is shown in Figure 2. All the spectra listed in Table 1 will be available on WISeREP (Yaron & Gal-Yam 2012). [Chang: Can't forget to do this, though it can wait until after the paper is accepted]

2.5. Near-Infrared Spectroscopy

We obtained one NIR (0.8–2.5 μm) spectrum of SN 2020jgb using the Gemini near-infrared spectrometer (GNIRS; Elias et al. 1998) on the Gemini North telescope on 2020 June 9 (~ 22 days after r_{ZTF} -band peak), with a total integration time of 2400 s. The GNIRS spectrum was reduced with `PyPeIt`.

3. ANALYSIS

3.1. Photometric Properties

SN 2020jgb exhibited a fainter light curve than normal SNe Ia. In Figure 1, we compare the photometric

³ <https://web.ipac.caltech.edu/staff/fmasci/ztf/forcedphot.pdf>

⁴ <https://www.not.iac.es/instruments/alfosc/>

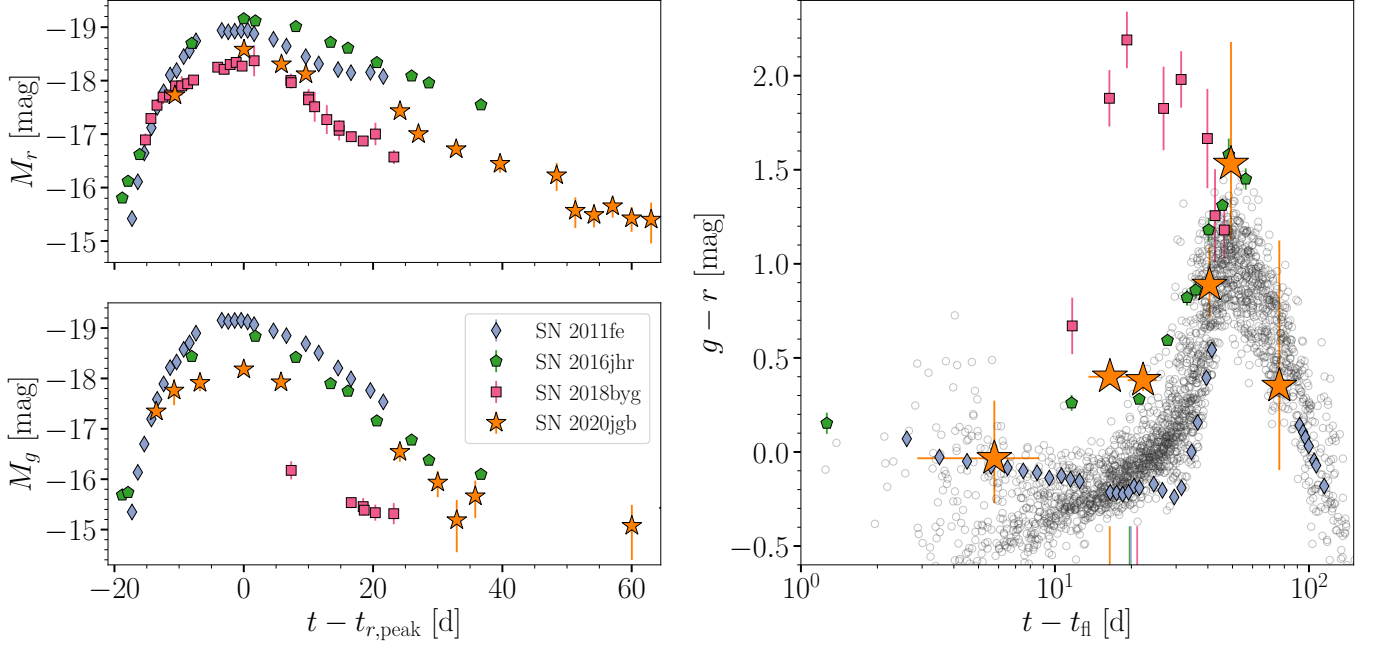


Figure 1. Comparison of the photometric properties of SN 2020jgb with those of SN 2011fe (normal SNe Ia; Pereira et al. 2013), SN 2016jhr (normal-luminosity He-shell DDet; Jiang et al. 2017), and SN 2018byg (subluminous He-shell DDet; De et al. 2019). *Left:* Multiband light curves. The upper (lower) panel shows the evolution in the r -band (g -band) absolute magnitude. *Right:* $g - r$ color evolution. For each object, the peak luminosity epoch is marked by a vertical line with the corresponding color on the bottom axis. The gray circles denote the $g_{\text{ZTF}} - r_{\text{ZTF}}$ color evolution of 62 normal SNe Ia (open circles) with prompt observations within 5 days of first light by ZTF (Bulla et al. 2020).

properties of SN 2020jgb with the nearby, well-observed SN 2011fe in g_{ZTF} and r_{ZTF} synthetic photometry from the spectrophotometric time series of Pereira et al. (2013), as well as two He-shell DDet candidates, including the normal-luminosity thin He-shell candidate SN 2016jhr (Jiang et al. 2017) and the subluminous thick He-shell candidate SN 2018byg (De et al. 2019). All of these light curves have been corrected for Galactic reddening, while K -corrections have not been performed⁵, because we do not have complete spectral sequences of these peculiar events.

While the observational coverage is sparse in the rise to maximum light, from Figure 1 it is clear that SN 2020jgb is less luminous than normal SNe Ia (e.g., SN 2011fe). If the host galaxy reddens SN 2020jgb by $E(B - V)_{\text{host}} = 0.13$ mag, then SN 2020jgb would be ~ 0.3 mag brighter in the r_{ZTF} band and ~ 0.5 mag in the g_{ZTF} band, making it comparable to SN 2011fe in r_{ZTF} , yet still ~ 0.5 mag fainter in g_{ZTF} . Furthermore, there is a flatter evolution in r_{ZTF} between -14 d and maximum light for both SN 2020jgb and SN 2018byg than there is for SN 2011fe.

⁵ These SNe were all observed in slightly different g and r filters.

In the right panel of Figure 1, we compare the color evolution ($g - r$) of these objects relative to the measured time of first light t_{fl} , accompanied by 62 normal SNe Ia (open circles) observed within 5 days of t_{fl} by ZTF (from Bulla et al. 2020). They have been corrected for Galactic extinction, but K -corrections have not been performed for consistency. For SN 2020jgb, the early rise of the light curve was not well sampled, so we estimate t_{fl} as the midpoint of the first detection and the last nondetection. We adopt an uncertainty in this estimate of 3 days. All three He-shell DDet candidates are undoubtedly redder than normal SNe Ia. At maximum light, SN 2020jgb ($g_{\text{ZTF}} - r_{\text{ZTF}} \approx 0.4$ mag) was not as red as SN 2018byg ($g - r \approx 2.2$ mag), but exhibited a similar color as SN 2016jhr ($g - r \approx 0.3$ mag). Adopting $E(B - V)_{\text{host}} = 0.13$ mag still results in a relatively red color for SN 2020jgb ($g_{\text{ZTF}} - r_{\text{ZTF}} \approx 0.2$ mag) compared to normal SNe Ia ($g_{\text{ZTF}} - r_{\text{ZTF}} \approx -0.1$ mag).

Interestingly, for both SN 2018byg and SN 2020jgb, near their maximum light the spectra sharply peak at ~ 5200 Å in the SN rest frame (see Figure 2), which is close to the red edge of the g/g_{ZTF} filter (~ 4000 – 5500 Å). Thus, modest redshifts ($z \gtrsim 0.03$) can produce significant K -corrections, which constitute a substantial fraction of the observed red $g - r$ colors for these events. For SN 2020jgb, using the ALFOSC spectrum

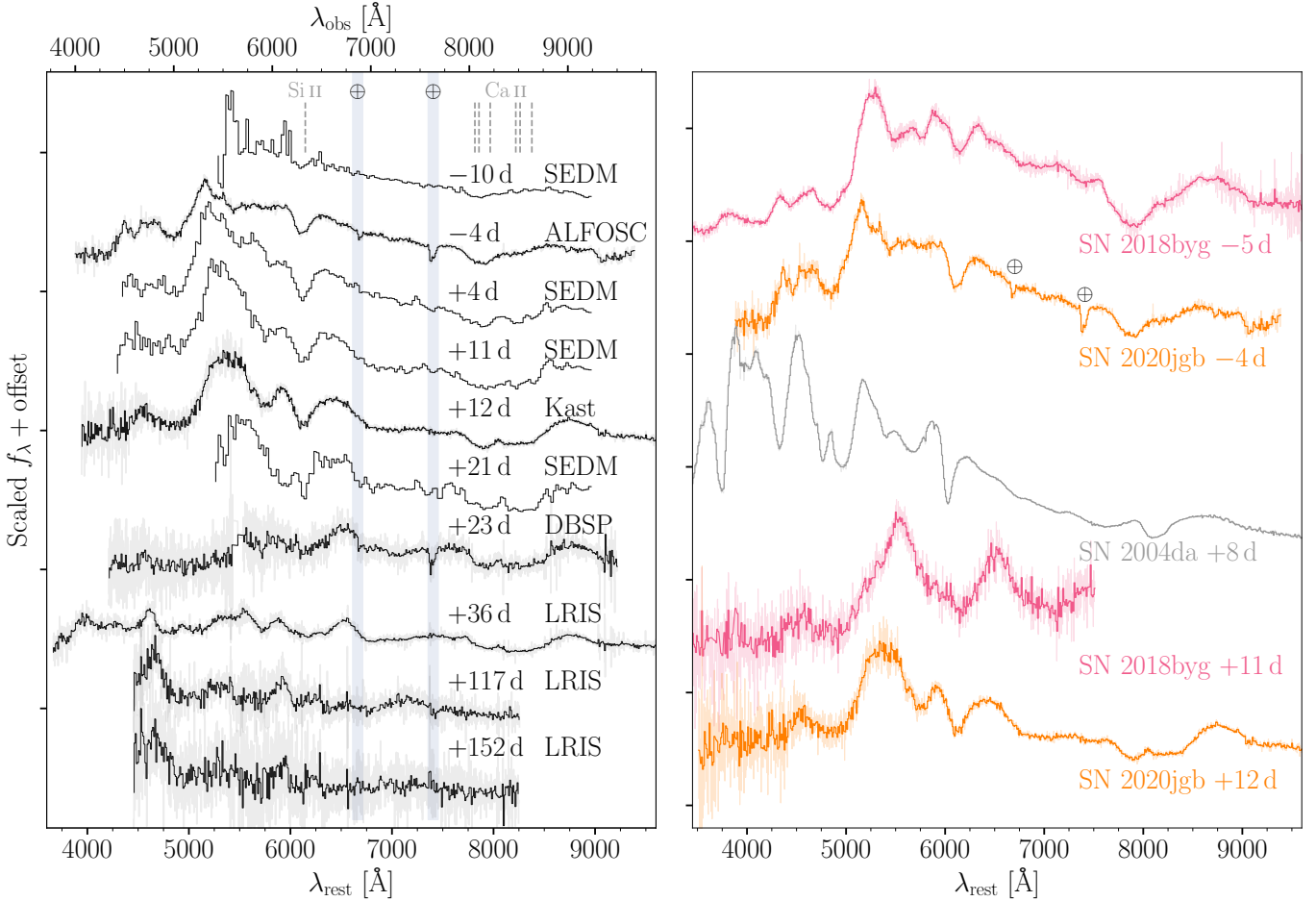


Figure 2. The optical spectral evolution of SN 2020jgb is typical of a peculiar SN Ia triggered by a He-shell DDet. *Left:* optical spectral sequence of SN 2020jgb. Rest-frame phases (days) relative to the r_{ZTF} -band peak and instruments used are posted next to each spectrum. Spectra have been corrected for $E(B-V)_{\text{MW}} = 0.404$ mag and are shown in gray. The black lines are binned spectra with a bin size of 10 \AA , except for the SEDM spectra, whose resolution is lower than the bin size. In the last two spectra, we have subtracted the light from the host galaxy. Only regions with $\text{SNR} > 2.5$ after binning are plotted. The corresponding wavelengths of the Si II $\lambda 6355$ line (with an expansion velocity of $10,000 \text{ km s}^{-1}$) and the Ca II IRT (with expansion velocities of both $10,000 \text{ km s}^{-1}$ and $25,000 \text{ km s}^{-1}$) are marked by the vertical dashed lines. *Right:* spectral comparison with SN 2018byg (subluminous He-shell DDet; De et al. 2019) and SN 2004da (normal luminosity; Silverman et al. 2012).

obtained at -4 d, we estimate the K -correction to be $K_{g-r} \approx -0.2$ mag, the $g-r$ color being bluer in the rest frame. SN 2018byg is at a higher redshift ($z = 0.066$) so the K -correction is more extreme ($K_{g-r} \approx -1.0$ mag). Future efforts to identify additional subluminous He-shell DDet candidates can utilize the red $g-r$ color to improve their search efficiency.

3.2. Optical Spectral Properties

In Figure 2, we show the optical spectral sequence of SN 2020jgb, and compare its spectra with those of some other SNe Ia at similar phases relative to peak brightness. For the spectra obtained after $+100$ d there is clear contamination from the host galaxy, including the presence of narrow emission lines. For these spectra we subtract the galaxy light as measured in the DEIMOS

spectrum from 2022 (see Section 2.4). The earliest spectrum was obtained by SEDM ~ 10 days before r_{ZTF} -band peak. We only show portions of the binned spectrum where the $\text{SNR} > 2.5$. The continuum is almost featureless with some marginal detection of the Si II $\lambda 6355$ at $\sim 6100 \text{ \AA}$, the hallmark of SNe Ia. In subsequent spectra the Si II features become more prominent and are clearly detected until ~ 12 days after maximum light. We measure Si II expansion velocities following a procedure similar to that of Childress et al. (2013, 2014) and Maguire et al. (2014). The fitting region is selected by visual inspection. The continuum is assumed to be linear, and the absorption profile after the continuum normalization is assumed to be composed of double Gaussian profiles centered at 6347 \AA and 6371 \AA . Within the model, the continuum flux density at the blue and red edges are free

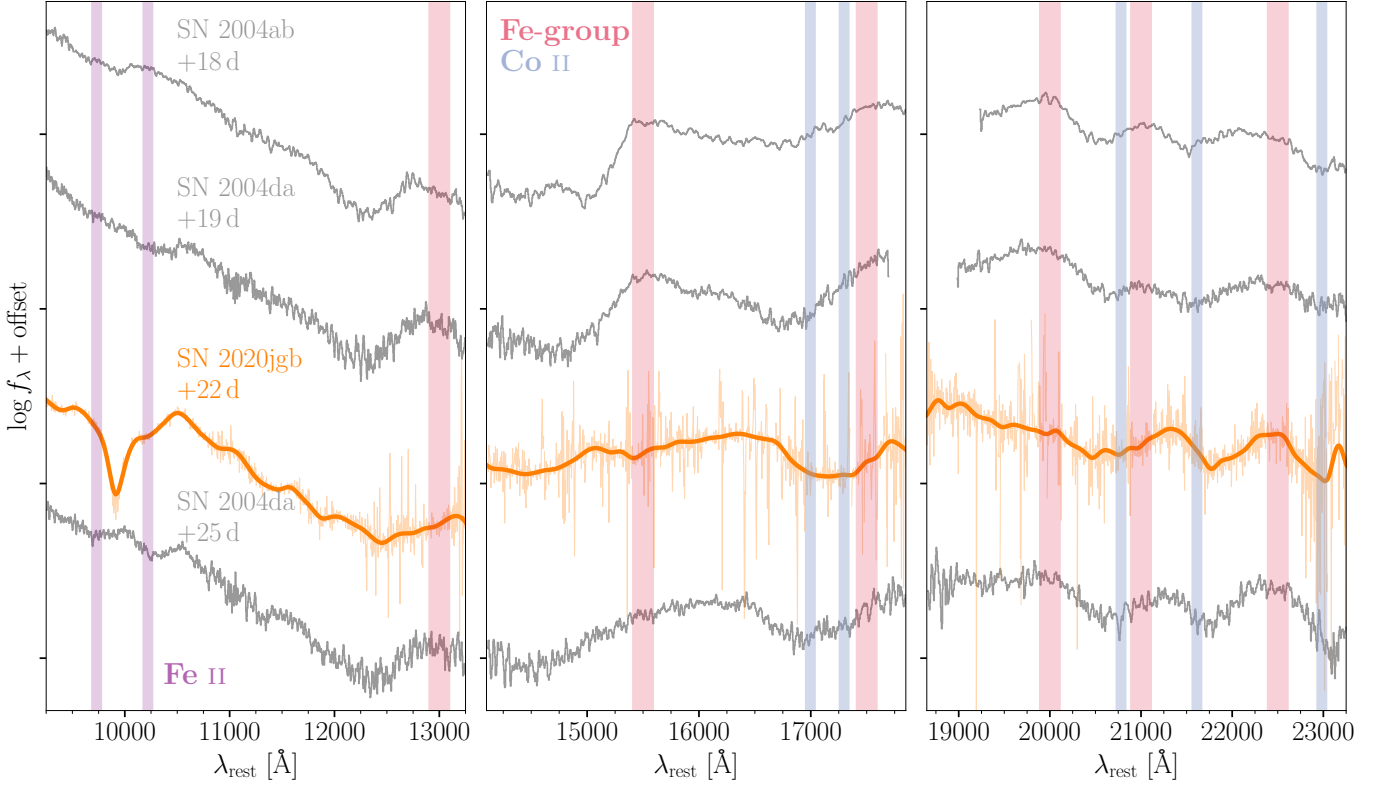


Figure 3. NIR spectra of SN 2020jgb and two normal-luminosity SNe Ia, SN 2004ab and SN 2004da (Marion et al. 2009), both showing highly similar spectral features except the absorption line near $1\,\mu\text{m}$. All spectra were obtained at similar phases. For each spectrum, the continuum at $\gtrsim 1.2\,\mu\text{m}$ is significantly reshaped by the line-blanketing from Fe-group elements (red stripes), which are continuous emission features composed of unresolved Fe-group lines peaking at $\sim 1.30, 1.55, 1.75, 2.00, 2.10$, and $2.25\,\mu\text{m}$ (Marion et al. 2009). Between these peaks lie multiple strong Co II absorption lines (blue stripes), for which a typical post-maximum expansion velocity of $8000\,\text{km s}^{-1}$ is assumed. The purple stripes correspond to Fe II $\lambda 9998$ and Fe II $\lambda 10500$, also with an expansion velocity of $8000\,\text{km s}^{-1}$.

parameters for which we adopt a normal distribution as a prior. The mean and standard deviation for the distribution are the observed flux density and its uncertainty (respectively) at each edge of the fitting region. Three more parameters (amplitude, mean velocity, logarithmic velocity dispersion) are used to characterize the double-Gaussian profile, whose priors are set to be flat. This means the depths and widths of both peaks are forced to be the same, as Maguire et al. (2014) adopted in the optically thick regime. The posteriors of the five parameters are sampled simultaneously with *emcee* (Foreman-Mackey et al. 2013) using the Markov chain Monte Carlo (MCMC) method. We find that the mean expansion velocity is $\sim 11,500\,\text{km s}^{-1}$ near maximum light.

SN 2020jgb does not show any absorption features associated with O I $\lambda 7774$. While the low luminosity, red color, absence of hydrogen features, and star-forming host galaxy of SN 2020jgb are reminiscent of Type Ic SNe (SNe Ic), which arise from stripped-envelope massive stars, SNe Ic usually exhibit stronger O I $\lambda 7774$

lines. The ratio of the relative line depths⁶ between the O I $\lambda 7774$ line and the Si II $\lambda 6355$ line is expected to be greater than 1 in typical SNe Ic (Sun & Gal-Yam 2017; Gal-Yam 2017). The absence of O I $\lambda 7774$ allows us to definitively conclude SN 2020jgb is not a SNe Ic.

In many SNe Ia, the Ca II near-infrared triplet (Ca II IRT) $\lambda\lambda 8498, 8542, 8662$ causes two distinct components (Mazzali et al. 2005), which are conventionally referred to as photospheric-velocity features (PVFs) and high-velocity features (HVs). The PVFs originate from the main line-forming region with typical photospheric (i.e., bulk ejecta) velocities, while the HVFs are blueshifted to much shorter wavelengths, indicating significantly higher (by $\gtrsim 6000\,\text{km s}^{-1}$) velocities than typical PVFs (Silverman et al. 2015). Figure 2 shows that SN 2020jgb has prominent HVFs of Ca II IRT. The HVFs are visible in our first spectrum of SN 2020jgb at $-10\,\text{d}$, and remain

⁶ The relative depth is defined as the absorption line depth relative to the pseudo-continuum. See Sun & Gal-Yam (2017) for more details.

prominent through +36 d. Using the same technique we use to model the Si II features, we fit the HVFs and PVFs simultaneously. Both are fit by multiple Gaussian profiles assuming each line in the triplet can be approximated by the same profile (i.e., same amplitude and velocity dispersion). A best-fit expansion velocity of HVFs at -10 d is $\sim 26,000 \text{ km s}^{-1}$. In the -4 d spectrum, we observe a clear delineation between the HVFs and PVFs. For this and subsequent spectra, we fit the broad absorption features with two different velocity components simultaneously. From -4 d to $+23$ d, the speed of the HVFs declines slightly to $\sim 24,000 \text{ km s}^{-1}$, and the speed of PVFs declines from $\sim 11,000 \text{ km s}^{-1}$ to $\sim 9,000 \text{ km s}^{-1}$. As in normal SNe Ia, the relative strength between the HVFs and PVFs decreases with time.

The optical spectral evolution of SN 2020jgb resembles that of SN 2018byg, a subluminal thick He-shell DDet SN. At early times, both SNe were relatively blue and featureless, with broad and shallow Ca II IRT absorption. As they evolved closer to maximum light, they developed strong continuous absorption blueward of $\sim 5000 \text{ \AA}$.⁷ Meanwhile, Si II $\lambda 6355$ and the Ca II IRT became more prominent. Neither O I nor S II was detected in either object. In the He-shell DDet scenario, a large amount of Fe-group elements would be synthesized in the shell, which would cause significant line-blanketing near maximum light (Kromer et al. 2010; Polin et al. 2019) and high-velocity intermediate-mass elements like Ca II (Fink et al. 2010; Kromer et al. 2010; Shen & Moore 2014). The similarity to SN 2018byg makes SN 2020jgb another promising He-shell DDet SN candidate.

SN 2004da is a normal SN Ia that shows similarities to SN 2020jgb in the NIR (Section 3.3); however, the two SNe are very different in the optical (Figure 2). From this comparison it is clear that SN 2020jgb is not a normal SN Ia.

We obtained two LRIS spectra at $+117$ d and $+152$ d, both of which are dominated by Fe-group elements and resemble those of normal SNe Ia (e.g., SN 2011fe; Mazzali et al. 2015), showing some enhancement in flux between ~ 4500 and $\sim 6000 \text{ \AA}$. There are no signs of emission due to the [Ca II] $\lambda\lambda 7291, 7324$ doublet.

3.3. NIR Spectral Properties

The NIR spectrum of SN 2020jgb is compared with those of two normal SNe Ia at a similar phase in Figure 3 (data for SN 2004ab and SN 2004da from Marion et al. 2009). SN 2020jgb shows a strong absorption fea-

ture at $\sim 0.99 \mu\text{m}$, which is not seen in normal SNe Ia. This feature was still significant two weeks later, as detected with LRIS on Keck (see Figure 6), though it was only partially covered. Aside from this prominent feature, SN 2020jgb resembles normal SNe Ia in the NIR. The shape of the continuum redward of $\sim 1.2 \mu\text{m}$ is significantly altered by line-blanketing from Fe-group elements. Just like normal SNe Ia, SN 2020jgb shows an enhancement of flux at about $1.30, 1.55, 2.00, 2.10$, and $2.25 \mu\text{m}$, accompanied by several Co II absorption lines. It is especially similar to SN 2004da at $+25$ d as the steep increase in flux at $\sim 1.55 \mu\text{m}$, known as the *H*-band break (Hsiao et al. 2019), has become less prominent. To summarize, the NIR spectrum of SN 2020jgb is dominated by Fe-group elements, consistent with the nucleosynthetic yield of a WD thermonuclear explosion. However, the $1 \mu\text{m}$ feature adds to the peculiarities of SN 2020jgb as a SN Ia.

Marion et al. (2009) presented a sample of 15 NIR spectra of normal SNe Ia between $+14$ and $+75$ d relative to maximum light, and none of those spectra show prominent absorption features around $1 \mu\text{m}$. We have investigated several potential identifications for this feature (see below), none of which provides a completely satisfying explanation.

The most tantalizing possibility is that the absorption is due to He I $\lambda 10830$. Modern DDet models reveal that part of the helium in the shell will be left unburnt (e.g., Kromer et al. 2010; Woosley & Kasen 2011; Polin et al. 2019). With full non-local thermodynamic equilibrium (LTE) physics taken into consideration, He I features are unambiguously expected in some He-shell DDet SNe, among which He I $\lambda 10830$ is the most prominent absorption line (Dessart & Hillier 2015; Boyle et al. 2017).⁸ [Chang: I wonder if it makes sense to have a footnote here saying that the formation of He lines requires non-LTE radiation transport, which is why Polin models (and Shen?) do not have He lines. Then another sentence noting that these models do show unburned He. Maybe that's also too much.] [AAM: One of our collaborators raised a related question: why didn't we model the NIR spectrum with SEDONA? It would be necessary to mention He I lines are non-LTE effects (people on Ib/c should be more familiar with this).] Figure 6 shows that the $1 \mu\text{m}$ feature, if associated with He I $\lambda 10830$, has a velocity of $\sim 26,000 \text{ km s}^{-1}$. This speed

⁷ This feature is prominent in SN 2020jgb when we adopt $E(B - V)_{\text{host}} = 0.0$ or 0.13 mag .

⁸ Since helium has high excitation states, optical and NIR helium lines require non-thermal excitation (e.g., collision with fast electrons; Lucy 1991). Models assuming LTE radiative transfer neglect non-thermal effects; thus, they are not able to characterize the helium features.

is consistent with the unburnt helium in He-shell DDet models when the ejecta have reached homologous expansion (Kromer et al. 2010; Polin et al. 2019), yet it is unclear whether the high-velocity unburnt helium could stay optically thick several weeks after maximum light. The Ca II IRT also exhibits similarly high velocities at the same phase ($\sim 24,000 \text{ km s}^{-1}$), meaning that high-velocity absorption is not impossible at this phase. The expansion velocity in the ejecta is roughly linearly proportional to the radius, so such a high velocity indicates that both the Ca II IRT and the tentative He I absorption line form far outside the normal photosphere, which has a velocity of only $\sim 10,000 \text{ km s}^{-1}$. The two-dimensional (2-D) models of Kromer et al. (2010) also suggest that helium may expand faster than the synthesized calcium in the He-shell. In this sense, the He-shell DDet scenario is supported because any unburnt helium would be located in the outermost ejecta.

We cannot claim an unambiguous detection of He I, however, as our spectra lack definitive absorption from other He I features that we would expect to be prominent, such as He I $\lambda 20581$. Considering a line velocity of $\sim 26,000 \text{ km s}^{-1}$ and a host-galaxy redshift of 0.0309, this line will be blueshifted to $\sim 1.95 \mu\text{m}$ in the observer frame, which overlaps with some strong telluric lines within $1.8\text{--}2.0 \mu\text{m}$. In this region our NIR spectrum has $\text{SNR} \approx 5$ following telluric correction, yet we do not see any significant absorption feature. An upper limit of the equivalent width is determined to be $<2\%$ that of the He I $\lambda 10830$ line, while theoretically, the $\lambda 20581$ line is supposed to be only a factor of 6–12 weaker, depending on the temperature (Marion et al. 2009). The observed $1 \mu\text{m}$ feature in SN 2020jgb is as strong as the He I $\lambda 10830$ line in many helium-rich Type Ib supernovae (SNe Ib; see Filippenko 1997; Gal-Yam 2017, for a review of SN spectral classification). In SNe Ib, the He I $\lambda 20581$ line is weaker than the He I $\lambda 10830$ line, yet still prominent (Shahbandeh et al. 2022). In one of the models of Boyle et al. (2017), there is no obvious He I $\lambda 20581$ absorption in the synthetic spectra (see their Figure 7), but the model is intended to be representative of normal-luminosity SNe Ia. If the $1 \mu\text{m}$ feature is associated with He I, it is unusual that we do not detect a corresponding feature around $2 \mu\text{m}$.

Other possible identifications for the $1 \mu\text{m}$ feature include Mg II $\lambda 10927$, C I $\lambda 10693$, and Fe II $\lambda 10500$ and $\lambda 10863$. The Mg II $\lambda 10927$ line is prevalent in the NIR spectra of SNe Ia, but usually disappears within a week after peak brightness (Marion et al. 2009). In SN 2020jgb the $1 \mu\text{m}$ feature was still visible more than a month after maximum light in the Keck/LRIS spectrum. A Mg II $\lambda 10927$ identification would require an

absorption velocity of $\sim 28,000 \text{ km s}^{-1}$, $\sim 20\%$ faster than the HVFs of Ca II IRT at the same phase. Such a high-velocity Mg II line has never been seen in other SNe Ia, and requires a high magnesium abundance in the outermost ejecta. However, the amount of magnesium synthesized in the detonation of the He-shell is expected to be tiny (Fink et al. 2010; Kromer et al. 2010; Polin et al. 2019, 2021). On the other hand, if we attribute this $1 \mu\text{m}$ feature to high-velocity Mg II, we would expect an even stronger Mg II $\lambda 9227$ line to be blueshifted to the red edge of the Ca II IRT, which is not detected. Given the strength of the $1 \mu\text{m}$ feature, the Mg II $\lambda 9227$ line should not be completely obscured by the Ca II IRT features.

C I $\lambda 10693$ is not observed as frequently as Mg II $\lambda 10927$ in SNe Ia. Hsiao et al. (2019) presented a sample of five SNe Ia with C I detections, showing that the C I feature is strongest for fainter, fast-declining objects. However, in their sample, the C I line is a pre-maximum feature which fades away as the luminosity peaks, so the discrepancy in phase is large. The required expansion velocity $\sim 22,000 \text{ km s}^{-1}$ is substantially faster than the estimated carbon velocity for the sample of Hsiao et al. (2019) ($\sim 10,000\text{--}12,000 \text{ km s}^{-1}$), but still consistent with the HVFs of Ca II IRT in SN 2020jgb. Nonetheless, no significant carbon absorption is detected in the optical. It is also noteworthy that the amount of unburnt carbon is expected to be minimal in sub- M_{Ch} WDs ignited by He-shell detonation (Polin et al. 2019), in contrast to near- M_{Ch} WDs ignited by pure deflagration where the carbon burning could be incomplete. We therefore would not expect to detect any carbon features in a He-shell DDet SN.

The Fe II features in SNe Ia usually start to develop approximately three weeks after peak brightness, which is about the same phase as we obtained our GNIRS spectrum. Two Fe II lines, $\lambda 9998$ and $\lambda 10500$, are actually visible on the blue/red wings of the $1 \mu\text{m}$ feature (see Figure 3). The Fe II $\lambda 10863$ line is not detected in the GNIRS spectrum. SN 2004da shows very similar Fe II features near $1 \mu\text{m}$, in which Fe II $\lambda 10500$ is the strongest line at this phase, as displayed in Figure 3. They correspond to an expansion velocity of $\sim 8000 \text{ km s}^{-1}$, which is consistent with the PVFs of the Ca II IRT at the same epoch. They also match the same two lines for normal SNe Ia (Marion et al. 2009), making the identification more reliable. Obviously, these two Fe II features are wider and shallower than the strong feature between them. We fit the $1 \mu\text{m}$ feature with three Gaussian profiles. Two of them are set to be the blueshifted Fe II $\lambda 9998$ and $\lambda 10500$, and the other is an uncorrelated Gaussian profile which mainly describes the deep

absorption feature in the center of the line complex. We find that the shallower and wider Fe II lines only make up $\sim 40\%$ of the total equivalent width, and the remaining $\sim 60\%$ comes from the central feature, which cannot be accounted for by any Fe II feature at the same velocity. Given the similarity of the Fe-group line-blanketing between the GNIRS spectrum with the spectrum of SN 2004da at +25 d, the distribution of Fe-group elements inside each SN ejecta should be somewhat similar, so the central region of the $1\ \mu\text{m}$ feature is not likely to be associated with Fe II either.

4. DISCUSSION

4.1. Models

We model SN 2020jgb using the methods outlined by Polin et al. (2019); the process is twofold. After choosing an initial model that describes a WD of a given mass with a choice of He-shell mass, we use the CASTRO code (Almgren et al. 2010) to perform a 1-D hydrodynamic simulation with simultaneous nucleosynthesis from the time of He-shell ignition through the secondary detonation and until the ejecta have reached homologous expansion (~ 10 s). At this point we take the ejecta profile (velocity, density, temperature and composition) and use the Monte Carlo radiative transport code SEDONA (Kasen et al. 2006) to calculate synthetic light curves and spectra of our model under the assumption of LTE.

For He-shell DDet SNe, the peak luminosity in r_{ZTF} is a proxy of the amount of ^{56}Ni synthesized in the detonation, which reflects the total progenitor mass (C/O core + He-shell; Polin et al. 2019). We find models with a total mass of $0.95\ M_{\odot}$ reproduce the r_{ZTF} -band peak brightness well if there is no extinction from the host galaxy. If the host galaxy reddens SN 2020jgb by $E(B - V)_{\text{host}} = 0.13\ \text{mag}$, then specific luminosity in r_{ZTF} would be $\sim 25\%$ higher, and the corresponding progenitor mass would be roughly $1.00\ M_{\odot}$. The uncertainty in the extinction limits the precision with which the progenitor mass of SN 2020jgb can be constrained.

Nonetheless, the major photometric and spectroscopic features of SN 2020jgb are consistent with those of a DDet SN with a massive shell. In Figure 4, we show the comparison of the observations of SN 2020jgb with thick He-shell ($0.13\ M_{\odot}$) DDet models with total masses of $0.95\ M_{\odot}$ and $1.00\ M_{\odot}$, respectively. To compare the models with the observations, we apply the adopted host reddening [$E(B - V)_{\text{host}} = 0.0$ or $0.13\ \text{mag}$] to the rest-frame model SN spectrum, then redshift the model spectrum by 0.0309 , before applying Galactic reddening [$E(B - V)_{\text{MW}} = 0.404\ \text{mag}$]. Both models reproduce the overall evolution of SN 2020jgb in r_{ZTF} , but fail to provide a reasonable fit to the light curve in g_{ZTF} . Specif-

ically, the peak brightness in g_{ZTF} is overestimated in the $0.87\ M_{\odot} + 0.13\ M_{\odot}$ model but underestimated in the $0.82\ M_{\odot} + 0.13\ M_{\odot}$ model. Then after maximum light in r_{ZTF} , both models show a rapidly declining g_{ZTF} -band light curve, which is $\gtrsim 1\ \text{mag}$ fainter than our observations at the same epoch.

The spectral comparison reveals more details. We find that both models, especially the $0.82\ M_{\odot} + 0.13\ M_{\odot}$ one, provide an excellent match to the ALFOSC spectrum obtained ~ 4 days prior to the peak at rest-frame wavelengths $\gtrsim 5500\ \text{\AA}$, including the Si II $\lambda 6355$ and multi-component Ca II IRT absorption features as well as the continuum. The same is true for the SEDM spectrum obtained ~ 4 days after peak light, though both models overpredict flux excess in the Ca II IRT P-Cygni profile. Meanwhile, both models provide a poor fit to the observation in bluer regions. Before peak light, the $0.87\ M_{\odot} + 0.13\ M_{\odot}$ model exhibits weaker Fe-group line-blanketing, thus showing a much higher total flux in g_{ZTF} . The $0.82\ M_{\odot} + 0.13\ M_{\odot}$ model provides a proper level of line-blanketing, but the continuous absorption in the synthetic spectrum terminates at a longer wavelength ($\sim 5400\ \text{\AA}$, as opposed to $\sim 5200\ \text{\AA}$ in the $-4\ \text{d}$ spectrum). As we have already mentioned in Section 3.1 when discussing K -corrections, the observed flux in g_{ZTF} is extremely sensitive to the red edge of the line-blanketing region, which, in the observer frame, is close to the edge of the filter. Figure 4 shows that while f_{λ} peaks in the g_{ZTF} filter near maximum light, in the $0.82\ M_{\odot} + 0.13\ M_{\odot}$ model the synthetic f_{λ} peaks in the gap between the g_{ZTF} and r_{ZTF} filters. The same is true for the $0.87\ M_{\odot} + 0.13\ M_{\odot}$ model after the r_{ZTF} -band peak. Interestingly, this mismatch is also seen when fitting similar DDet models to SN 2018byg (see Figure 6 in De et al. 2019) despite the convincing match to observations at longer wavelengths, suggesting this is one of the systematics in our models. By manually shifting the synthetic spectra at $-4\ \text{d}$ in the $0.82\ M_{\odot} + 0.13\ M_{\odot}$ model blueward by $200\ \text{\AA}$, we find that the corresponding synthetic magnitude in g_{ZTF} immediately increases by $\sim 0.5\ \text{mag}$. Given the sensitivity of brightness in g_{ZTF} on modeling the line-blanketing and the uncertainty in our models from Polin et al. (2019), we do not attempt to fit the g_{ZTF} -band light curve of SN 2020jgb even near maximum light.

The systematics in modeling the line-blanketing (and the flux in many similar g bands) may be attributed to a variety of factors on handling the explosion and radiative transfer. First, our models assume local thermodynamic equilibrium (LTE), which is not valid once the ejecta become optically thin. Typically the bulk ejecta of a sub- M_{Ch} SNIa remain optically thick for

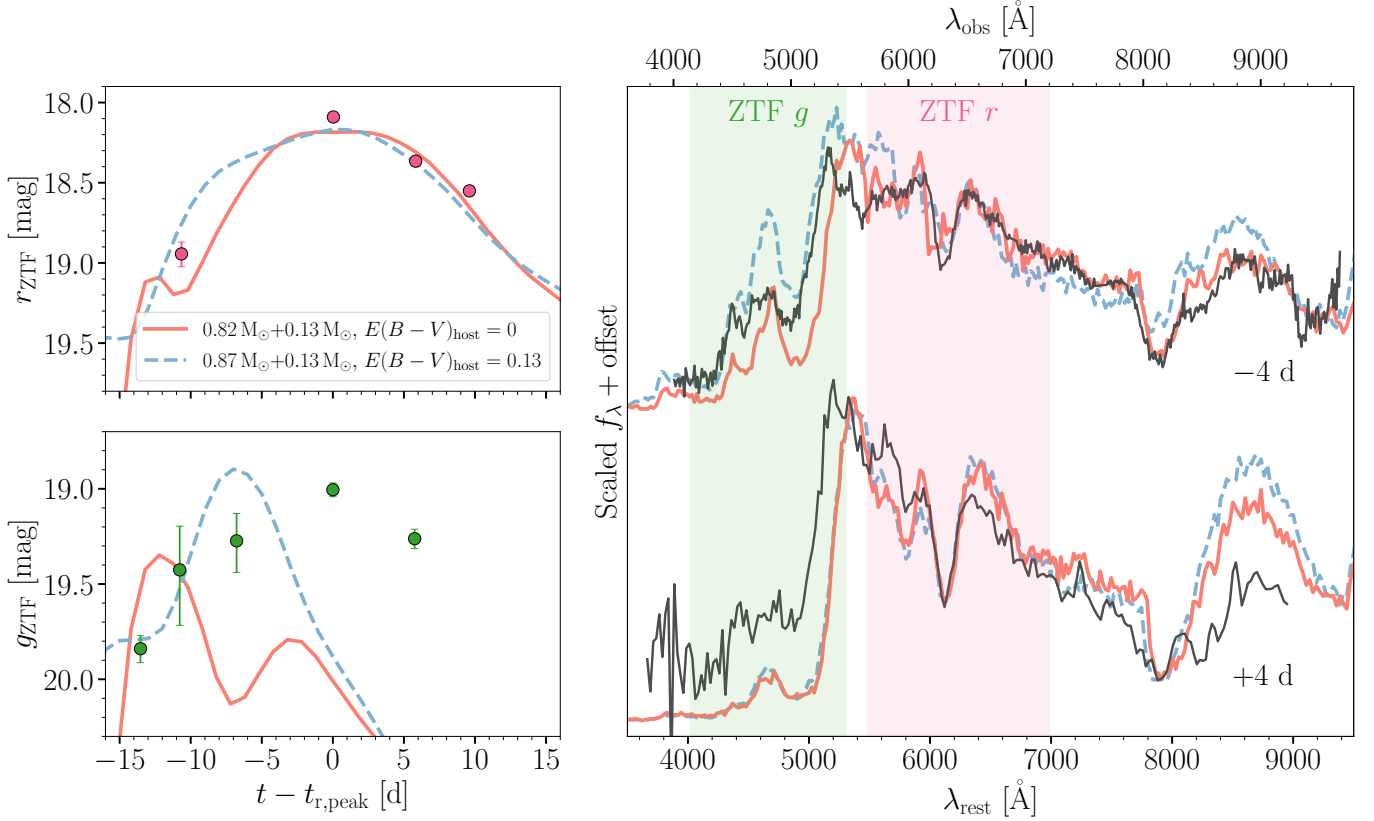


Figure 4. Spectrophotometric comparison of SN 2020jgb observations with two thick He-shell DDet models using the methods described in Polin et al. (2019). For the $0.82 M_{\odot} + 0.13 M_{\odot}$ model, only the Galactic reddening of $E(B - V)_{\text{MW}} = 0.404$ mag is applied to the synthetic spectra and photometry; for the $0.87 M_{\odot} + 0.13 M_{\odot}$ model, additional reddening of $E(B - V)_{\text{host}} = 0.13$ mag from the host galaxy is assumed. *Left:* Comparison of the ZTF photometry with the synthetic light curves. The model parameters are indicated in the legend as (C/O core mass + He-shell mass). The upper (lower) panel shows the evolution in r_{ZTF} (g_{ZTF}). The phases have been rescaled to the host-galaxy rest frame. *Right:* Comparison of the observed spectra with the models around peak luminosity. The shaded regions correspond to the coverage of the ZTF g and r filters with transmission above half maximum. All spectra are normalized such that they would have a same synthetic brightness in r_{ZTF} . The synthetic spectra are further binned with a size of 20 \AA .

~ 30 days after the explosion. But in modeling the g_{ZTF} -band brightness, the LTE assumption is more challenging because the major opacity in g_{ZTF} comes from the Fe-group line-blanketing in the outermost ejecta, where the optical depth may evolve differently from that near the photosphere. Hence, the LTE condition may become inapplicable much earlier. Furthermore, our 1-D He-shell model is not capable of capturing multidimensional effects in the explosion such as asymmetries. The viewing angle is known to have a significant influence on the observed light curves (Kromer et al. 2010; Sim et al. 2012; Gronow et al. 2020; Shen et al. 2021), especially in bluer bands where the line-blanketing depends sensitively on the distribution of He-shell ashes (Shen et al. 2021). In previous studies of other He-shell DDet objects, the g -band brightness is systematically under-predicted shortly after the peak, despite the fact that

redder bands can be fit decently (e.g., Jiang et al. 2017; Jacobson-Galán et al. 2020).

Another discrepancy occurs in the late-time spectra. It is argued in Polin et al. (2021) that as the total progenitor mass in the He-shell DDet decreases, the SN gets fainter and the major coolants in the nebular phase change smoothly from Fe-group elements to the [Ca II] $\lambda\lambda 7291, 7324$ doublet. Nebular [Ca II] emission is a hallmark for Ca-rich transients and is prominent in the Ca-Ia objects (Galbany et al. 2019; De et al. 2020). For a total progenitor mass $\lesssim 1.0 M_{\odot}$, [Ca II] emission features are expected to dominate Fe-group features, clearly in contrast to what we see in SN 2020jgb. This suggests that either SN 2020jgb suffers a substantial amount of host reddening, such that the actual progenitor mass is $\gtrsim 1.0 M_{\odot}$; or the transition between the Fe-strong and Ca-strong regimes occurs for a lower progenitor mass than simulations have predicted. The Ca-Ia object

SN 2016hnk is estimated to have an even lower progenitor mass ($\sim 0.87 M_{\odot}$; Jacobson-Galán et al. 2020) and shows [Ca II] lines indisputably, drawing a lower limit of the progenitor mass for this transition (c.f., Galbany et al. 2019, for discussion on the potential host galaxy extinction on SN 2016hnk). While the thick He-shell DDet events SN 2018byg and SN 2016dsg lack significant [Ca II] emission, all of the available spectra for these SNe were obtained $\lesssim +50$ d, well before these SNe have fully transitioned to the nebular phase.

Given the strong match in the r_{ZTF} -band light curves and the near-peak spectra at wavelengths $\gtrsim 5500$ Å between the observations of SN 2020jgb and our He-shell DDet models following Polin et al. (2019), we conclude that SN 2020jgb is consistent with a DDet event ignited by a massive He-shell. The readers are referred to our Appendix A where we show the comparison of our observations to models with a variety of shell masses, in which the thinner-shell models (shell masses $< 0.1 M_{\odot}$) cannot reproduce the properties of SN 2020jgb. Depending on the extinction in the host galaxy, the total mass of the progenitor should be ~ 0.95 – $1.00 M_{\odot}$. To constrain the progenitor masses of additional He-shell DDet SNe to a higher precision, one should thoroughly discuss any potential host extinction. Multidimensional simulations with more realistic radiative transfer setups are necessary to resolve the systematics in our current models.

4.2. The $1 \mu\text{m}$ Feature

While the nature of the $1 \mu\text{m}$ feature remains uncertain, other He-shell DDet candidates show similar complexity in this region. In the currently small sample, only three objects (SN 2016hnk, SN 2018byg, and SN 2020jgb) have at least one available NIR spectrum (all obtained at different phases), yet each exhibits a strong absorption feature near $1 \mu\text{m}$, as shown in Figure 5. SN 2016hnk has two deep absorption features at $\sim 1.02 \mu\text{m}$ and $\sim 1.17 \mu\text{m}$. It is suggested in Galbany et al. (2019) that both of them are caused by Fe II, though they are deeper than in other SNe Ia. The velocity of the $1.02 \mu\text{m}$ feature is $\sim 21,000 \text{ km s}^{-1}$ assuming a He I $\lambda 10830$ origin, which, just like for SN 2020jgb, is about the same as the HVFs of the Ca II IRT (see Figure 6). The PVFs of the Ca II IRT of both SNe have a similar expansion velocity of $\sim 10,000 \text{ km s}^{-1}$. Such a consistency in velocities is also seen in SN 2018byg (see Figure 6). The large width and low SNR for the $1 \mu\text{m}$ feature in SN 2018byg make it difficult to determine an exact line velocity. The feature may be a mixture of several different lines in SN 2018byg.

Dong et al. (2022a) recently presented another thick He-shell DDet candidate, SN 2016dsg, with an absorp-

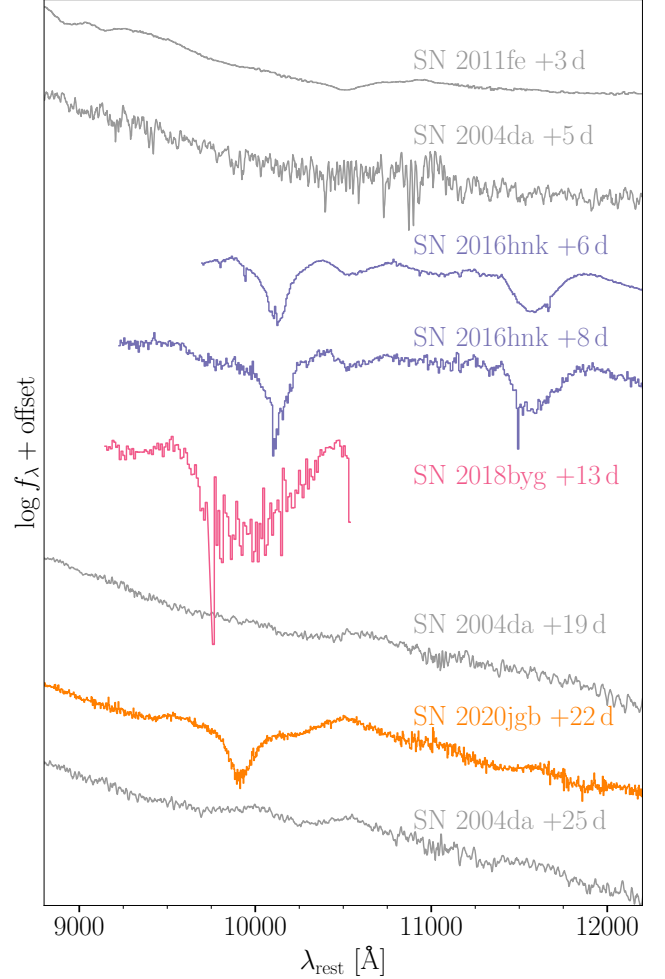


Figure 5. NIR spectra of normal SNe Ia SN 2011fe (Mazali et al. 2014) and SN 2004da (Marion et al. 2009) and three subluminal SNe Ia as He-shell DDet candidates — SN 2016hnk (Galbany et al. 2019), SN 2018byg (De et al. 2019), and SN 2020jgb (this work). All three He-shell DDet candidates show prominent absorption near $1 \mu\text{m}$. The spectrum of SN 2018byg is originally noisy, so it is binned with a size of 10 Å .

tion line around 0.97 – $1.05 \mu\text{m}$ in a low-SNR NIR spectrum at $+16.6$ d.⁹ Assuming a He I $\lambda 10830$ origin, the minimum of the absorption profile (at $\sim 1.03 \mu\text{m}$; see Figure 4 of Dong et al. 2022a) corresponds to an expansion velocity of $\sim 15,000 \text{ km s}^{-1}$. Interestingly, SN 2016dsg shows the least prominent Ca II IRT HVFs ($v_{\text{SN 2016dsg}} \approx 15,000 \text{ km s}^{-1}$) among all the He-shell DDet candidates with NIR spectra. Once again, the scenario where both the unburnt helium and the high-

⁹ SN 2016dsg was discovered on the decline. The phase is relative to the discovery time.

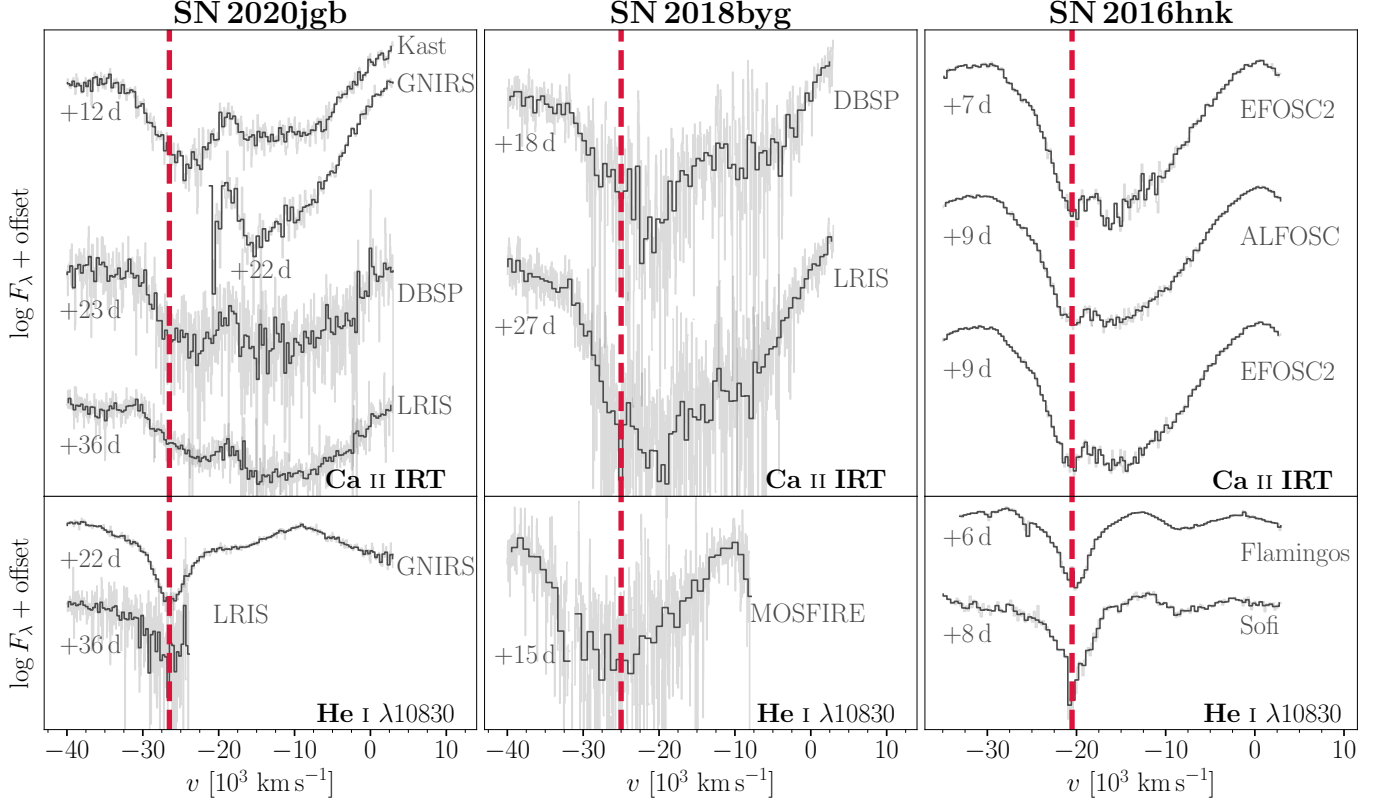


Figure 6. Spectra of SN 2020jgb, SN 2018byg (De et al. 2019), and SN 2016hbk (Galbany et al. 2019) in velocity space, showing the similarity in expansion velocities of the $1\,\mu\text{m}$ features (lower panels) with the Ca II IRT absorption features (upper panels), assuming the $1\,\mu\text{m}$ features are associated with He I $\lambda 10830$. The red dashed lines mark the minimum of each $1\,\mu\text{m}$ feature, which are displayed to guide the eye.

velocity calcium are located at the outermost shell is favored.

Unfortunately, none of the spectra of SN 2016dsg, SN 2016hbk, or SN 2018byg cover the $2\,\mu\text{m}$ region; thus, it is not possible to identify the presence of helium decisively. But if the $1\,\mu\text{m}$ features of these objects are of the same origin, they are more likely to be correlated with the high-velocity ejecta lying in the outmost region in the SNe, because at least for SN 2020jgb, SN 2016dsg, and SN 2016hbk, the difference in their photospheric velocities cannot explain the discrepancy in their line velocities of the $1\,\mu\text{m}$ feature. Then helium is still a promising candidate to cause strong absorption near $1\,\mu\text{m}$ for these subluminal He-shell DDet SNe Ia.

In conclusion, every thick He-shell DDet candidate with available NIR spectra displays a strong absorption feature near $1\,\mu\text{m}$.¹⁰

This feature is not seen in normal SNe Ia. Interestingly, the available NIR spectra are all obtained at different epochs, suggesting that this feature may be long lived. If the feature is due to He I, then DDet explosions exhibit a wide diversity in the expansion velocity. While it remains to be confirmed in a larger sample, we speculate that anomalously strong absorption around $1\,\mu\text{m}$ is a distinctive attribute of He-shell DDet SNe and that this feature can be used to identify and select events relative to normal SNe Ia.

4.3. The Host Environment of He-Shell DDet SNe

¹⁰ We also note that a similar $1\,\mu\text{m}$ feature is detected in another possibly relevant object, SN 2012hn (Valenti et al. 2014), in a NIR spectrum obtained at +25 d. SN 2012hn is a Ca-rich transient exhibiting weak Si II lines and no optical helium features (a Ca-Ic object in the classification scheme in De et al. 2020). It shows similar spectral properties (e.g., Fe-group line-blanking) to those of the two Ca-Ia objects (De et al. 2020). This indicates a possible He-shell DDet origin of SN 2012hn.

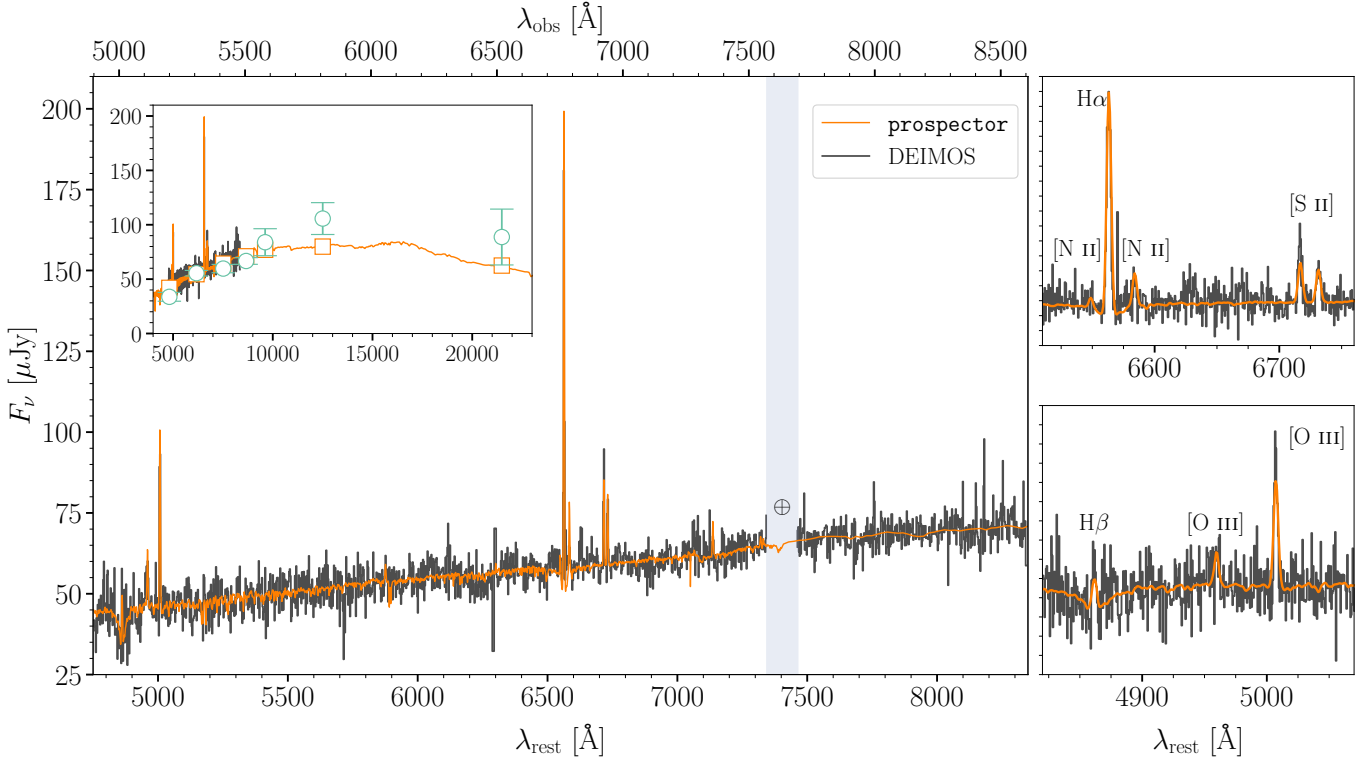


Figure 7. The SED of the star-forming dwarf galaxy PSO J175312.663+005122.078 (the host galaxy of SN 2020jgb) and the model from **prospector**. When fitting the SED with **prospector**, the DEIMOS spectrum is automatically rescaled to fit the archival photometry from Pan-STARRS (Chambers et al. 2016, g , r , i , z , y Kron magnitudes) and VHS (McMahon et al. 2013, J and K_s Petrosian magnitudes). *Left:* the SED in the optical band (4750–8350 Å in the rest frame of the host galaxy). The black line corresponds to the observed spectrum, binned with a size of 2 Å. The orange line is the **prospector** model produced from the median of the stellar population property posterior distributions. The blue shaded region is masked in the fitting owing to the strong telluric lines. *Inner panel:* the same comparison, but covering the g through K_s bands (4000–24,000 Å). Apart from the spectra, we also show the multiband photometry (green circles) and the best-fit magnitudes (orange squares). *Right:* spectra around the most prominent emission lines. *Top right:* H α , [N II] $\lambda\lambda$ 6548, 6583, [S II] $\lambda\lambda$ 6716, 6731. *Bottom right:* H β , [O III] $\lambda\lambda$ 4959, 5007.

We model the host galaxy of SN 2020jgb using **prospector** (Johnson et al. 2021), a package for principled inference of stellar population properties using photometric and/or spectroscopic data. **Prospector** applies a nested sampling fitting routine through **dynesty** (Speagle 2020) to the observed data and produces posterior distributions of the stellar population properties and model spectral energy distributions (SEDs) with use of **Python-FSPS** (Conroy et al. 2009; Conroy & Gunn 2010). Our observed data include the Galactic-extinction-corrected DEIMOS spectrum, as well as the archival photometric data from the Panoramic Survey Telescope and Rapid Response System (Pan-STARRS; Chambers et al. 2016, g , r , i , z , y Kron magnitudes) and the VISTA Hemisphere Survey (VHS; McMahon et al. 2013, J and K_s Petrosian magnitudes). We use a parametric delayed- τ star-formation history, given by Equation (1) of Nugent et al. (2020) and defined by the e -folding factor τ , the Galactic dust extinction law

(Cardelli et al. 1989), and the Chabrier initial mass function (Chabrier 2003) to the model. We further apply a mass-metallicity relation (Gallazzi et al. 2005) to sample realistic stellar masses and metallicities and a dust law that ensures young stellar light attenuates dust twice the amount of old stellar light, as has been observed. We also add a nebular emission model (Byler et al. 2017) with a gas-phase metallicity and a gas ionization parameter to correctly measure the strength of the emission lines in the DEIMOS spectrum. The model spectral continuum is built from a tenth-order Chebyshev polynomial. We determine the stellar mass and star-formation rate (SFR) from the **prospector** output, as shown by Nugent et al. (2022). The estimated stellar mass is $\log(M_* [M_\odot]) = 7.79^{+0.07}_{-0.06}$, and the specific star-formation rate (sSFR) is $\log(\text{sSFR} [\text{yr}^{-1}]) = -10.25^{+0.09}_{-0.08}$, with the uncertainties denoting the 68% highest posterior density regions.

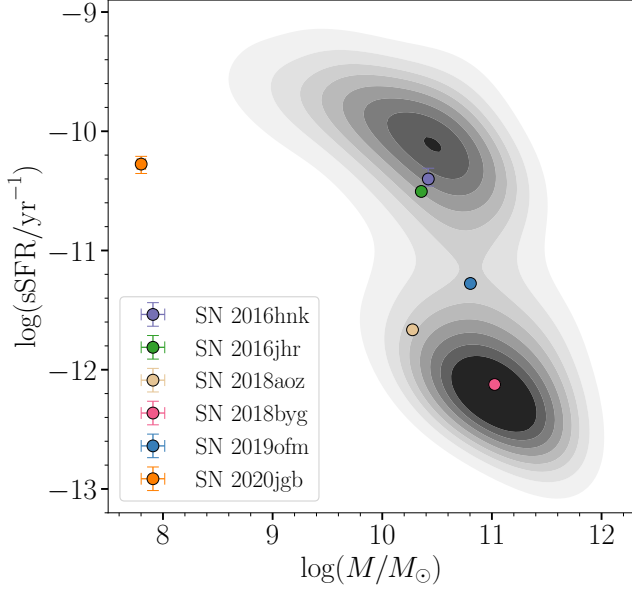


Figure 8. The sSFR and stellar mass for the host galaxies of He-shell DDet candidates, showing that He-shell DDet SNe can emerge in both star-forming and passive galaxies. The properties for the hosts of SN 2016hmk and SN 2018aoz are taken from Dong et al. (2022b) and the CLU catalog (Cook et al. 2019; De et al. 2020), respectively. The gray contours correspond to the bivariate distributions of stellar mass and sSFR for galaxies in the SDSS MPA-JHU DR8 catalog (Kauffmann et al. 2003; Brinchmann et al. 2004), visualized using kernel density estimation (KDE) with the data visualization library `seaborn` (Waskom 2021). Galaxies with BPT classification as AGNs or LINERs are excluded, since certain spectral features (e.g., H α emission) due to nuclear activity might be misinterpreted as being caused by star formation.

In Figure 8, we show the sSFR and the stellar mass for the host galaxies of six He-shell DDet candidates. Again using `prospector`, we fit the stellar properties for all the other candidates with optical spectra from the Sloan Digital Sky Survey (SDSS; York et al. 2000) and photometry from the DESI Legacy Imaging Surveys Data Release 9 (DR9) (LS; Dey et al. 2019, g , r , z , W_1 , W_2 , W_3 , W_4 magnitudes). With mid-infrared (MIR) photometry¹¹ available, `prospector` can better estimate the overall dust extinction in the host galaxy and the contribution of an active galactic nucleus (AGN) to the SED. We therefore add two additional parameters to our `prospector` fit to sample the MIR optical depth

¹¹ LS DR9 includes MIR (W_1 – W_4) fluxes from images through year 6 of NEOWISE-Reactivation (https://wise2.ipac.caltech.edu/docs/release/neowise/neowise.2020_release_intro.html) force-photometered in the unWISE (Meisner et al. 2018) maps at the locations of LS optical sources.

and fraction of the total galaxy luminosity due to an AGN.

[AAM: A question on footnotes: it seems that they should appear BEFORE commas and AFTER full stops, is that correct?] [Chang: I had always been taught after punctuation NEVER before - commas and periods should never be “on an island”]

Unfortunately, two hosts (those of the two Ca-Ia objects SN 2016hmk and SN 2019ofm) are nearby ($z \lesssim 0.03$) late-type galaxies with extended, spatially resolved spiral structures. Examination of the photometry model from Legacy Surveys (LS) shows that the galaxy aperture does not include the blue, diffuse star-forming regions of these galaxies. Fitting the SDSS spectra + LS photometry would inevitably underestimate their sSFR. For the host of SN 2016hmk, we instead adopt the results of Dong et al. (2022b), which are based on broadband far-ultraviolet (FUV) to far-infrared (FIR) photometry from the $z = 0$ Multiwavelength Galaxy Synthesis I (z0MGS; Leroy et al. 2019) to characterize the stellar population with `prospector`. The SFR they estimated is 1.1 dex higher than ours, suggesting intense star-formation in the spiral arms. For the host of SN 2019ofm, there are no archival stellar population data available; so we redo the photometry using science-ready coadded images from the *Galaxy Evolution Explorer* (GALEX) general release 6/7 (Martin et al. 2005, FUV and NUV bands), SDSS DR 9 (Ahn et al. 2012, u , g , r , i , z bands), the Two Micron All Sky Survey (2MASS; Skrutskie et al. 2006, H and J bands), and preprocessed WISE images (Wright et al. 2010) from the unWISE archive (Lang 2014, W_1 and W_2 bands).¹² We use the software package LAMBDA (Lambda Adaptive Multi-Band Deblending Algorithm in R) (Wright 2016) and tools presented in Schulze et al. (2021), to measure the total brightness of the host galaxy. But with the LAMBDA photometry, the estimated SFR is essentially the same as in the previous fit, suggesting that there is not much ongoing star-formation in the spiral arms. This, along with its moderate sSFR ($\log(\text{sSFR} [\text{yr}^{-1}]) = -11.27$), indicates the host galaxy is in the transitional phase.

In addition, the host of the normal SN Ia SN 2018aoz (NGC 3923) is a local ($z = 0.00580$) early-type galaxy and is outside the SDSS footprint, so we adopt its stellar population properties from the Census of the Local Universe (CLU) catalog (Cook et al. 2019; De et al. 2020).

¹² The unWISE images are based on the public WISE data and include images from the ongoing NEOWISE-Reactivation mission R3 (Mainzer et al. 2014; Meisner et al. 2017), available on <http://unwise.me>.

The other Ca-Ia object PTF 09dav is not displayed in Figure 8 because it appears to be hostless, with the nearest galaxy with a known redshift being a star-forming late-type galaxy ~ 40 kpc away (Sullivan et al. 2011). Nonetheless, it is close to several extended sources with low surface brightness, which could be faint dwarf galaxies (see Figure 3 in Kasliwal et al. 2012). Its nebular-phase spectrum exhibits $H\alpha$ emission, which indicates potential star formation, but could also be explained with photoionized gas around the transient (Kasliwal et al. 2012).

Figure 8 reveals that He-shell DDet SNe emerge in both star-forming and passive galaxies. There is also significant diversity in their location within their host galaxy. SN 2020jgb has a small projected physical offset (~ 0.2 kpc) from the center of its host, a star-forming dwarf galaxy, so it is likely to originate from a young, star-forming environment. SN 2016hmk has a moderate projected host offset (~ 4 kpc) and a potential origin in an H II region with ongoing star formation (Galbany et al. 2019). SN 2019ofm has a large projected offset (~ 11 kpc) but is still on a spiral arm, as shown in its DECaLS image (Dey et al. 2019). Other objects, including the recently reported SN 2016dsg and OGLE-2013-SN-079 (Dong et al. 2022a), show large projected host offsets ($\gtrsim 10$ kpc) and lie in the galaxy outskirts, which usually indicates an old stellar population origin.

In this sense, the He-shell DDet sample resembles the normal SNIa population, which can occur in both star-forming and quenched galaxies (e.g., Sullivan et al. 2006; Smith et al. 2012). This is very different from some other types of thermonuclear SNe such as Type-Iax SNe (SNeIax), which almost only appear in star-forming galaxies, or 91bg-like and SN 2002es-like (02es-like; Ganeshalingam et al. 2012) objects, which prefer old stellar environments (see the review by Jha et al. 2019). This favors the postulated sequence that He-shell DDet SNe may make up a substantial fraction of normal SNeIa, and is supported by stellar-metallicity observations (Sanders et al. 2021; Eitner et al. 2022).

The diversities in host environments indicate multiple formation channels in the He-shell DDet SN population. Those in star-forming galaxies, SN 2020jgb being the most unambiguous example, could originate from some analogues of the two subdwarf B binaries with WD companions (Geier et al. 2013; Kupfer et al. 2022) discovered in young stellar populations. On the other hand, those with large host offsets could not be easily formed *in situ*. Similarly, many Ca-rich transients are also observed in remote locations (e.g., Lunnan et al. 2017), for which some dynamical formation channels have been proposed (Lyman et al. 2014). To reach the outskirts of galax-

ies, WD binaries would need to be ejected by globular clusters (Shen et al. 2019) or supermassive black holes (Foley 2015) before explosion. Given that some Ca-rich transients show characteristic DDet properties (De et al. 2020), these channels may also be applicable to some of the He-shell DDet SNe.

The robust detection of SN 2020jgb in a star-forming region also agrees with independent studies of SNIa progenitors using stellar-metallicity observations. After measuring the manganese abundance in the Sculptor dwarf spheroidal galaxy, it is argued in de los Reyes et al. (2020) that sub- M_{Ch} SNeIa dominate the initial chemical enrichment of a galaxy, while near- M_{Ch} SNe become more important at later times. This indicates that observationally, sub- M_{Ch} SNeIa might have a stronger preference toward younger stellar populations than near- M_{Ch} SNeIa. We note that while SN 2020jgb is the first confirmed subluminous He-shell DDet SN in a star-forming dwarf, which indicates that thick He-shell DDet SNe might be intrinsically rare, the same may not be true for those ignited by a thin He-shell since they would look just as “normal” a few days after explosion (Magee et al. 2021). Unfortunately, few normal SNeIa have been observed at such an early phase to date; thus, we might have missed a great number of thin He-shell DDet SNe. A systematic study based on prompt follow-up observations of infant SNeIa will help verify this implication.

5. CONCLUSIONS

We have presented observations of SN 2020jgb, a peculiar SNIa. It has a low luminosity, red $g_{\text{ZTF}} - r_{\text{ZTF}}$ colors, and strong line-blanketing in the optical spectra near maximum light. These observational properties are highly similar to SN 2018byg (De et al. 2019), which could be explained by the detonation of a shell of helium on a sub- M_{Ch} WD. Fitting the light curves of SN 2020jgb to a grid of models from Polin et al. (2019), we show that a $\sim 0.82 M_{\odot}$ WD beneath a $\sim 0.13 M_{\odot}$ He-shell provides a reasonable match to the observed spectrophotometric evolution of SN 2020jgb. The uncertainty in the host galaxy extinction limits the precision on estimating total progenitor mass, with a reasonable upper limit being $\sim 1.00 M_{\odot}$.

A high-SNR NIR spectrum obtained three weeks after maximum light exhibits a prominent absorption feature near $1 \mu\text{m}$, which could be produced by the unburnt helium (He I $\lambda 10830$) in the outermost ejecta expanding at a high velocity ($\sim 26,000 \text{ km s}^{-1}$). At the same epoch, the Ca II IRT also has similarly high velocities ($\sim 24,000 \text{ km s}^{-1}$). To date, only a handful of candidate He-shell DDet SNe have observed NIR spectra. Inter-

estingly, all of them show deep absorption features near $1\ \mu\text{m}$, which, if assumed to be He I $\lambda 10830$, would be expanding at a very similar velocity to the HVFs of Ca II IRT. For these candidates the Ca II HVFs and putative He I velocities show significant diversity ranging from $\sim 15,000\ \text{km s}^{-1}$ in SN 2016dsg to $\sim 24,000\ \text{km s}^{-1}$ in SN 2020jgb. If it is the unburnt helium and the newly synthesized calcium from the He-shell that produce these line features, such a consistency in the expansion rates of different absorption lines would be naturally explained. However, we could not find unambiguous evidence for other He I absorption lines, such as He I $\lambda 20581$, so we cannot claim a definitive detection of helium in SN 2020jgb. Nonetheless, alternative possibilities (Mg II, C I, Fe II) that may cause the $1\ \mu\text{m}$ feature are deemed even less likely. Helium is thus the most plausible explanation for the apparently ubiquitous $1\ \mu\text{m}$ features.

We propose that He-shell DDet SNe can be robustly identified with NIR spectra. For transients showing a clear $1\ \mu\text{m}$ feature, to test its potential association with He I $\lambda 10830$ one could follow the checklist below.

- Search for He I $\lambda 20581$. A caveat is that one should not always expect to see significant He I $\lambda 20581$ absorption in He-shell DDet SNe, since this line is weaker than He I $\lambda 10830$ and could be almost invisible when the He-shell is thin (Boyle et al. 2017). Strong telluric lines near $2\ \mu\text{m}$ can make it difficult to detect He I $\lambda 20581$.
- Calculate the line velocity assuming the feature is He I $\lambda 10830$ and check if the speed is comparable with the Ca II IRT HVFs at a similar phase. While both the detonation recipe and viewing angles would affect the observed He I/Ca II velocity, we still expect both elements to expand at similar speeds along the line of sight if they all have a He-shell origin.
- Exclude the possibility of other strong lines. If the NIR spectrum is obtained before the peak brightness of the SN, strong Mg II and C I absorption (Hsiao et al. 2019) would be possible contaminants. Otherwise, if the $1\ \mu\text{m}$ feature is seen in the transitional-phase spectrum when the inner region of the SN becomes visible, we need to carefully rule out the possibility of an Fe II origin (Marion et al. 2009).

The small, but growing, sample of He-shell DDet SNe are heterogeneous in their observational properties, including peak luminosity, color evolution, chemical abundances, and line velocities, which could be explained by

a large variety of He-shell and WD masses (Polin et al. 2019; Shen et al. 2021), viewing angles (Shen et al. 2021), and the initial chemical compositions in the He-shell (Kromer et al. 2010). In addition, they are discovered in both old and young stellar populations, SN 2020jgb being the first unambiguous subluminal, thick He-shell DDet candidate in a star-forming galaxy. If, as has been argued (e.g., Sanders et al. 2021; Eitner et al. 2022), a substantial fraction of normal SNe Ia are triggered by He-shell DDet, then we would naturally expect He-shell DDet SNe to emerge in both star-forming and passive galaxies. Our discovery of SN 2020jgb in a star-forming dwarf galaxy confirms that He-shell DDet events occur in a variety of different galaxies. This is unlike some other subtypes of SNe Ia (Jha et al. 2019) which strongly prefer either star-forming galaxies (e.g., SNe Iax) or passive galaxies (e.g., 91bg-like and 02es-like objects). Nonetheless, it remains to be examined whether thick He-shell DDet SNe stem from similar progenitors as the normal SNe Ia triggered by the detonation of a thin He-shell, or if their massive He-shells could only be developed in a completely distinctive population of binary systems.

We thank Eddie Schlafly and Dustin Lang for suggesting photometry from DESI Legacy Imaging Surveys in SED fitting. We are grateful to Aishwarya Dahiwalé, Jillian Rastinejad, and Yuhao Yao for the high-quality spectra they obtained. We also appreciate the excellent assistance of the staffs of the various observatories where data were obtained. K.D. acknowledges support from NASA through the NASA Hubble Fellowship grant #HST-HF2-51477.001 awarded by the Space Telescope Science Institute, which is operated by the Association of Universities for Research in Astronomy, Inc., for NASA, under contract NAS5-26555. A.V.F. is grateful for financial support from the Christopher R. Redlich Fund and many other individual donors. K.M. is funded by the EU H2020 ERC grant No. 758638. S.S. acknowledges support from the G.R.E.A.T research environment, funded by *Vetenskapsrådet*, the Swedish Research Council, project number 2016-06012. The Keck II time was provided by CIERA/Northwestern.

This work is based on observations obtained with the Samuel Oschin Telescope 48-inch and the 60-inch Telescope at the Palomar Observatory as part of the Zwicky Transient Facility project. ZTF is supported by the National Science Foundation under Grant No. AST-1440341 and a collaboration including Caltech, IPAC, the Weizmann Institute of Science, the Oskar Klein Center at Stockholm University, the University of Maryland, the University of Washington, Deutsches Elektronen-

Synchrotron and Humboldt University, Los Alamos National Laboratories, the TANGO Consortium of Taiwan, the University of Wisconsin at Milwaukee, and Lawrence Berkeley National Laboratories. Operations are conducted by COO, IPAC, and UW. [Chang: this is out of date - Northwestern should be included in this acknowledgement] [AAM: But not in 2020 right?] [Chang: Was there guidance listed about this somewhere?]

SED Machine is based upon work supported by the National Science Foundation under Grant No. 1106171.

This work is also based on observations made with the Nordic Optical Telescope, owned in collaboration by the University of Turku and Aarhus University, and operated jointly by Aarhus University, the University of Turku and the University of Oslo, representing Denmark, Finland and Norway, the University of Iceland and Stockholm University at the Observatorio del Roque de los Muchachos, La Palma, Spain, of the Instituto de Astrofísica de Canarias.

A major upgrade of the Kast spectrograph on the Shane 3m telescope at Lick Observatory, led by Brad Holden, was made possible through gifts from the Heising-Simons Foundation, William and Marina Kast,

and the University of California Observatories. Research at Lick Observatory is partially supported by a generous gift from Google. The W. M. Keck Observatory is operated as a scientific partnership among the California Institute of Technology, the University of California and NASA; the observatory was made possible by the generous financial support of the W. M. Keck Foundation.

This work was also supported by the GROWTH project (Kasliwal et al. 2019) funded by the National Science Foundation under Grant No 1545949.

Facility: PO:1.2m (ZTF), PO:1.5m (SEDM), Gemini:Gillett (GNIRS), Hale (DBSP), NOT (ALFOSC), Shane (Kast Double spectrograph), Keck:I (LRIS), Keck:II (DEIMOS).

Software: `astropy` (Astropy Collaboration et al. 2013, 2018), `CASTRO` (Almgren et al. 2010), `dynesty` (Speagle 2020), `emcee` (Foreman-Mackey et al. 2013), `LAMBDA` (Wright 2016), `matplotlib` (Hunter 2007), `prospector` (Johnson et al. 2021), `PyPeIt` (Prochaska et al. 2020), `pysedm` (Rigault et al. 2019), `Python-FSPS` (Conroy et al. 2009; Conroy & Gunn 2010), `scipy` (Virtanen et al. 2020), `seaborn` (Waskom 2021), `SEDONA` (Kasen et al. 2006).

APPENDIX

A. COMPARISON TO DDET MODELS WITH VARIOUS SHELL MASSES

We have shown that the r_{ZTF} -band light curve and the observed spectra of SN 2020jgb near peak light are fairly consistent with the DDet of a sub- M_{Ch} WD beneath a massive shell ($\sim 0.13 M_{\odot}$), whose total mass is $\sim 0.95\text{--}1.00 M_{\odot}$. In this appendix we compare SN 2020jgb to other DDet models developed using the methods in Polin et al. (2019).

Figure 9 shows multiple models with a total mass of $\sim 0.95 M_{\odot}$, all of which reproduce the brightness of SN 2020jgb in r_{ZTF} if there is no host extinction. The g_{ZTF} -band synthetic light curves, which depend on the strength of the Fe-group elements line-blanketing, differ significantly depending on the helium shell mass. In the two models with thinner shells ($\lesssim 0.08 M_{\odot}$), the suppression of flux blueward to $\sim 5000 \text{ \AA}$ is much less significant than that seen in SN 2020jgb at -4 d . As a result, they overestimate the brightness in g_{ZTF} before maximum light. The $0.84 M_{\odot} + 0.11 M_{\odot}$ model shows the most significant line blanketing. [AAM: I was told I would need to explain the behavior of all the models used in the paper, at least qualitatively ; These arguments are based on what Abi said on the slack - maybe we can ask her for some references if necessary. For now I'll comment them out.]

Figure 10 shows models with a total mass of $\sim 1.00 M_{\odot}$ assuming $E(B - V)_{\text{host}} = 0.13 \text{ mag}$. Each model reproduces the brightness of SN 2020jgb in r_{ZTF} . The model with the thinnest shell significantly underestimates the level of line-blanketing, allowing us to eliminate it as a viable model for SN 2020jgb. Models with shells $\gtrsim 0.05 M_{\odot}$ exhibit similar behavior, meaning the shell mass is quite uncertain. Nonetheless, models with shells $\gtrsim 0.10 M_{\odot}$ better reproduce the velocity of the HVs of Ca II IRT before maximum light, which is underestimated in the $0.95 M_{\odot} + 0.05 M_{\odot}$ model. We note that all the $1.00 M_{\odot}$ -models overestimate the maximum brightness of SN 2020jgb in g_{ZTF} and underestimate the level of line blanketing in the -4 d spectrum.

While none of the models presented here provide a perfect match to the observations, it is clear that SN 2020jgb is consistent with thick-shell He DDet models (shell masses $\gtrsim 0.1 M_{\odot}$).

REFERENCES

- | | |
|--|---|
| <p>Ahn, C. P., Alexandroff, R., Allende Prieto, C., et al. 2012, ApJS, 203, 21, doi: 10.1088/0067-0049/203/2/21</p> | <p>Almgren, A. S., Beckner, V. E., Bell, J. B., et al. 2010, ApJ, 715, 1221, doi: 10.1088/0004-637X/715/2/1221</p> |
|--|---|

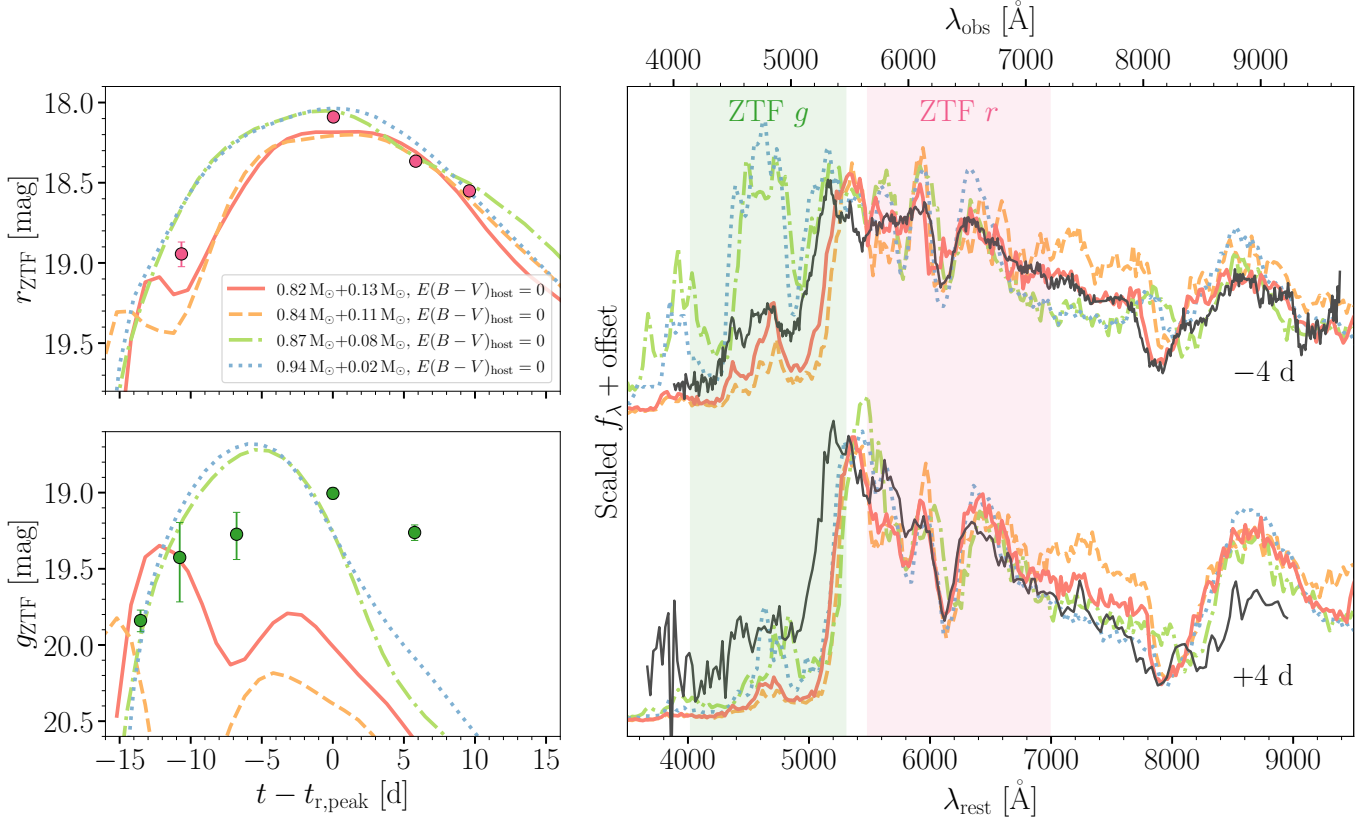


Figure 9. Similar to Figure 4, but more models with a total mass of $\sim 0.95 M_{\odot}$ and various shell masses (from $0.02 M_{\odot}$ to $0.13 M_{\odot}$) are displayed. For these models, we assume no host extinction.

Astropy Collaboration, Robitaille, T. P., Tollerud, E. J., et al. 2013, *A&A*, 558, A33, doi: [10.1051/0004-6361/201322068](https://doi.org/10.1051/0004-6361/201322068)

Astropy Collaboration, Price-Whelan, A. M., Sipőcz, B. M., et al. 2018, *AJ*, 156, 123, doi: [10.3847/1538-3881/aabc4f](https://doi.org/10.3847/1538-3881/aabc4f)

Baldwin, J. A., Phillips, M. M., & Terlevich, R. 1981, *PASP*, 93, 5, doi: [10.1086/130766](https://doi.org/10.1086/130766)

Bellm, E. C., Kulkarni, S. R., Graham, M. J., et al. 2019a, *PASP*, 131, 018002, doi: [10.1088/1538-3873/aaecbe](https://doi.org/10.1088/1538-3873/aaecbe)

Bellm, E. C., Kulkarni, S. R., Barlow, T., et al. 2019b, *PASP*, 131, 068003, doi: [10.1088/1538-3873/ab0c2a](https://doi.org/10.1088/1538-3873/ab0c2a)

Blagorodnova, N., Neill, J. D., Walters, R., et al. 2018, *PASP*, 130, 035003, doi: [10.1088/1538-3873/aaa53f](https://doi.org/10.1088/1538-3873/aaa53f)

Blondin, S., & Tonry, J. L. 2007, *ApJ*, 666, 1024, doi: [10.1086/520494](https://doi.org/10.1086/520494)

Boyle, A., Sim, S. A., Hachinger, S., & Kerzendorf, W. 2017, *A&A*, 599, A46, doi: [10.1051/0004-6361/201629712](https://doi.org/10.1051/0004-6361/201629712)

Brinchmann, J., Charlot, S., White, S. D. M., et al. 2004, *MNRAS*, 351, 1151, doi: [10.1111/j.1365-2966.2004.07881.x](https://doi.org/10.1111/j.1365-2966.2004.07881.x)

Bulla, M., Miller, A. A., Yao, Y., et al. 2020, *ApJ*, 902, 48, doi: [10.3847/1538-4357/abb13c](https://doi.org/10.3847/1538-4357/abb13c)

Byler, N., Dalcanton, J. J., Conroy, C., & Johnson, B. D. 2017, *ApJ*, 840, 44, doi: [10.3847/1538-4357/aa6c66](https://doi.org/10.3847/1538-4357/aa6c66)

Cardelli, J. A., Clayton, G. C., & Mathis, J. S. 1989, *ApJ*, 345, 245, doi: [10.1086/167900](https://doi.org/10.1086/167900)

Carrick, J., Turnbull, S. J., Lavaux, G., & Hudson, M. J. 2015, *MNRAS*, 450, 317, doi: [10.1093/mnras/stv547](https://doi.org/10.1093/mnras/stv547)

Cenko, S. B., Fox, D. B., Moon, D.-S., et al. 2006, *PASP*, 118, 1396, doi: [10.1086/508366](https://doi.org/10.1086/508366)

Chabrier, G. 2003, *PASP*, 115, 763, doi: [10.1086/376392](https://doi.org/10.1086/376392)

Chambers, K. C., Magnier, E. A., Metcalfe, N., et al. 2016, *arXiv e-prints*, arXiv:1612.05560, <https://arxiv.org/abs/1612.05560>

Childress, M. J., Filippenko, A. V., Ganeshalingam, M., & Schmidt, B. P. 2014, *MNRAS*, 437, 338, doi: [10.1093/mnras/stt1892](https://doi.org/10.1093/mnras/stt1892)

Childress, M. J., Scalzo, R. A., Sim, S. A., et al. 2013, *ApJ*, 770, 29, doi: [10.1088/0004-637X/770/1/29](https://doi.org/10.1088/0004-637X/770/1/29)

Conroy, C., & Gunn, J. E. 2010, *ApJ*, 712, 833, doi: [10.1088/0004-637X/712/2/833](https://doi.org/10.1088/0004-637X/712/2/833)

Conroy, C., Gunn, J. E., & White, M. 2009, *ApJ*, 699, 486, doi: [10.1088/0004-637X/699/1/486](https://doi.org/10.1088/0004-637X/699/1/486)

Cook, D. O., Kasliwal, M. M., Van Sistine, A., et al. 2019, *ApJ*, 880, 7, doi: [10.3847/1538-4357/ab2131](https://doi.org/10.3847/1538-4357/ab2131)

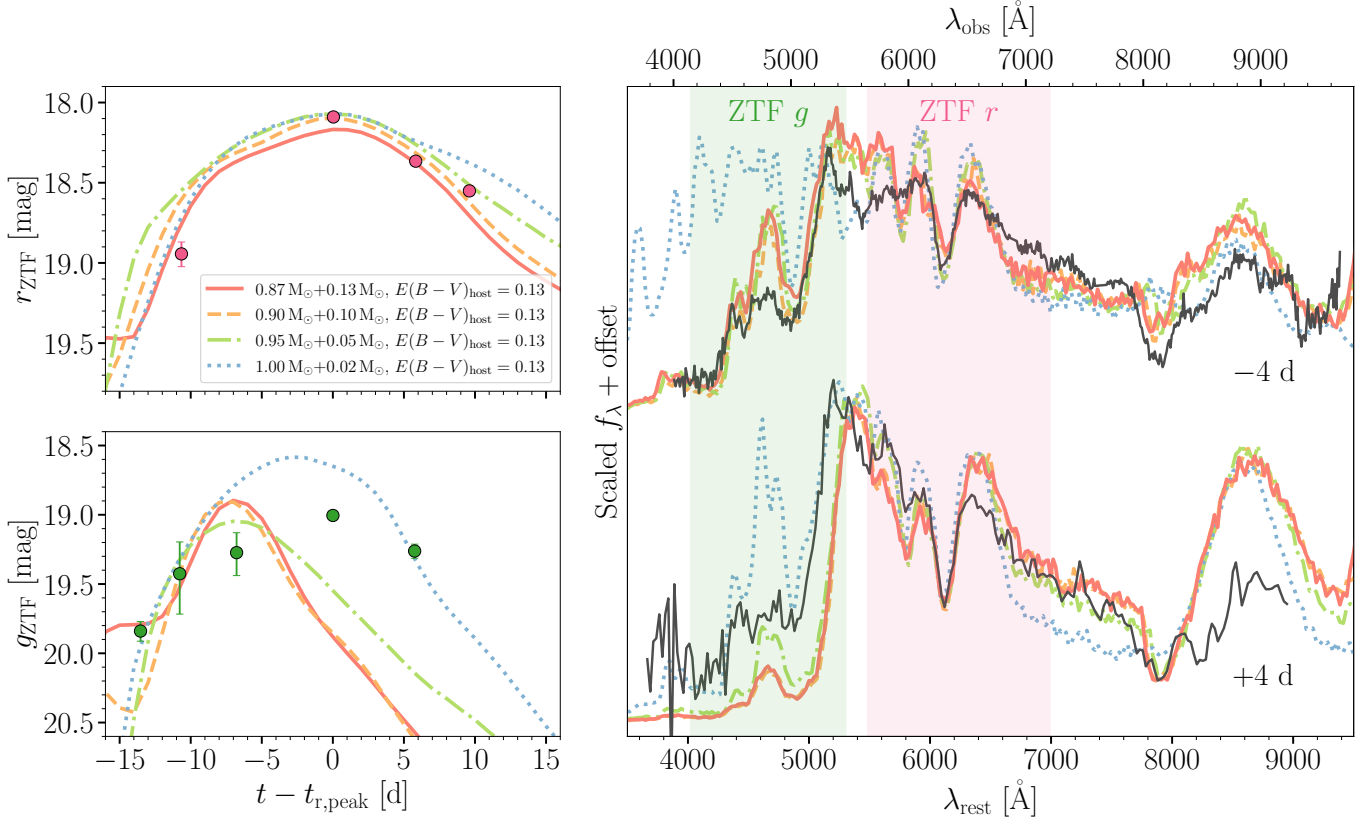


Figure 10. Similar to Figure 4, but more models with a total mass of $\sim 1.00 M_{\odot}$ and various shell masses (from $0.02 M_{\odot}$ to $0.13 M_{\odot}$) are displayed. For these models, we assume $E(B - V)_{\text{host}} = 0.13$.

Dahiwal, A., & Fremling, C. 2020, Transient Name Server Classification Report, 2020-1624, 1

De, K., Kasliwal, M. M., Polin, A., et al. 2019, The Astrophysical Journal, 873, L18, doi: [10.3847/2041-8213/ab0aec](https://doi.org/10.3847/2041-8213/ab0aec)

De, K., Kasliwal, M. M., Tzanidakis, A., et al. 2020, The Astrophysical Journal, 905, 58, doi: [10.3847/1538-4357/abb45c](https://doi.org/10.3847/1538-4357/abb45c)

De, K., Kasliwal, M. M., Tzanidakis, A., et al. 2020, ApJ, 905, 58, doi: [10.3847/1538-4357/abb45c](https://doi.org/10.3847/1538-4357/abb45c)

de los Reyes, M. A. C., Kirby, E. N., Seitzzahl, I. R., & Shen, K. J. 2020, ApJ, 891, 85, doi: [10.3847/1538-4357/ab736f](https://doi.org/10.3847/1538-4357/ab736f)

Deckers, M., Maguire, K., Magee, M. R., et al. 2022, MNRAS, 512, 1317, doi: [10.1093/mnras/stac558](https://doi.org/10.1093/mnras/stac558)

Dekany, R., Smith, R. M., Riddle, R., et al. 2020, PASP, 132, 038001, doi: [10.1088/1538-3873/ab4ca2](https://doi.org/10.1088/1538-3873/ab4ca2)

Dessart, L., & Hillier, D. J. 2015, MNRAS, 447, 1370, doi: [10.1093/mnras/stu2520](https://doi.org/10.1093/mnras/stu2520)

Dey, A., Schlegel, D. J., Lang, D., et al. 2019, AJ, 157, 168, doi: [10.3847/1538-3881/ab089d](https://doi.org/10.3847/1538-3881/ab089d)

Dong, Y., Valenti, S., Polin, A., et al. 2022a, arXiv e-prints, arXiv:2206.07065. <https://arxiv.org/abs/2206.07065>

Dong, Y., Milisavljevic, D., Leja, J., et al. 2022b, ApJ, 927, 199, doi: [10.3847/1538-4357/ac5257](https://doi.org/10.3847/1538-4357/ac5257)

Duev, D. A., Mahabal, A., Masci, F. J., et al. 2019, MNRAS, 489, 3582, doi: [10.1093/mnras/stz2357](https://doi.org/10.1093/mnras/stz2357)

Eitner, P., Bergemann, M., Ruiter, A. J., et al. 2022, arXiv e-prints, arXiv:2206.10258. <https://arxiv.org/abs/2206.10258>

Elias, J. H., Vukobratovich, D., Andrew, J. R., et al. 1998, in Society of Photo-Optical Instrumentation Engineers (SPIE) Conference Series, Vol. 3354, Infrared Astronomical Instrumentation, ed. A. M. Fowler, 555–565, doi: [10.1117/12.317281](https://doi.org/10.1117/12.317281)

Faber, S. M., Phillips, A. C., Kibrick, R. I., et al. 2003, in Society of Photo-Optical Instrumentation Engineers (SPIE) Conference Series, Vol. 4841, Instrument Design and Performance for Optical/Infrared Ground-based Telescopes, ed. M. Iye & A. F. M. Moorwood, 1657–1669, doi: [10.1117/12.460346](https://doi.org/10.1117/12.460346)

Filippenko, A. V. 1997, ARA&A, 35, 309, doi: [10.1146/annurev.astro.35.1.309](https://doi.org/10.1146/annurev.astro.35.1.309)

Filippenko, A. V., Chornock, R., Swift, B., et al. 2003, IAUC, 8159, 2

- Filippenko, A. V., Richmond, M. W., Branch, D., et al. 1992, *AJ*, 104, 1543, doi: [10.1086/116339](https://doi.org/10.1086/116339)
- Fink, M., Röpke, F. K., Hillebrandt, W., et al. 2010, *A&A*, 514, A53, doi: [10.1051/0004-6361/200913892](https://doi.org/10.1051/0004-6361/200913892)
- Fitzpatrick, E. L. 1999, *PASP*, 111, 63, doi: [10.1086/316293](https://doi.org/10.1086/316293)
- Foley, R. J. 2015, *MNRAS*, 452, 2463, doi: [10.1093/mnras/stv789](https://doi.org/10.1093/mnras/stv789)
- Foreman-Mackey, D., Hogg, D. W., Lang, D., & Goodman, J. 2013, *PASP*, 125, 306, doi: [10.1086/670067](https://doi.org/10.1086/670067)
- Fremling, C. 2020, *Transient Name Server Discovery Report*, 2020-1247, 1
- Gal-Yam, A. 2017, in *Handbook of Supernovae*, ed. A. W. Alsabti & P. Murdin, 195, doi: [10.1007/978-3-319-21846-5_35](https://doi.org/10.1007/978-3-319-21846-5_35)
- Galbany, L., Ashall, C., Höflich, P., et al. 2019, *Astronomy & Astrophysics*, 630, A76, doi: [10.1051/0004-6361/201935537](https://doi.org/10.1051/0004-6361/201935537)
- Gallazzi, A., Charlot, S., Brinchmann, J., White, S. D. M., & Tremonti, C. A. 2005, *MNRAS*, 362, 41, doi: [10.1111/j.1365-2966.2005.09321.x](https://doi.org/10.1111/j.1365-2966.2005.09321.x)
- Ganeshalingam, M., Li, W., Filippenko, A. V., et al. 2012, *ApJ*, 751, 142, doi: [10.1088/0004-637X/751/2/142](https://doi.org/10.1088/0004-637X/751/2/142)
- Geier, S., Marsh, T. R., Wang, B., et al. 2013, *A&A*, 554, A54, doi: [10.1051/0004-6361/201321395](https://doi.org/10.1051/0004-6361/201321395)
- Graham, M. J., Kulkarni, S. R., Bellm, E. C., et al. 2019, *PASP*, 131, 078001, doi: [10.1088/1538-3873/ab006c](https://doi.org/10.1088/1538-3873/ab006c)
- Gronow, S., Collins, C., Ohlmann, S. T., et al. 2020, *A&A*, 635, A169, doi: [10.1051/0004-6361/201936494](https://doi.org/10.1051/0004-6361/201936494)
- Hsiao, E. Y., Phillips, M. M., Marion, G. H., et al. 2019, *PASP*, 131, 014002, doi: [10.1088/1538-3873/aae961](https://doi.org/10.1088/1538-3873/aae961)
- Hunter, J. D. 2007, *Computing in Science and Engineering*, 9, 90, doi: [10.1109/MCSE.2007.55](https://doi.org/10.1109/MCSE.2007.55)
- Inserra, C., Sim, S. A., Wyrzykowski, L., et al. 2015, *ApJL*, 799, L2, doi: [10.1088/2041-8205/799/1/L2](https://doi.org/10.1088/2041-8205/799/1/L2)
- Jacobson-Galn, W. V., Polin, A., Foley, R. J., et al. 2020, *The Astrophysical Journal*, 896, 165, doi: [10.3847/1538-4357/ab94b8](https://doi.org/10.3847/1538-4357/ab94b8)
- Jha, S. W., Maguire, K., & Sullivan, M. 2019, *Nature Astronomy*, 3, 706, doi: [10.1038/s41550-019-0858-0](https://doi.org/10.1038/s41550-019-0858-0)
- Jiang, J.-a., Doi, M., Maeda, K., et al. 2017, *Nature*, 550, 80, doi: [10.1038/nature23908](https://doi.org/10.1038/nature23908)
- Johnson, B. D., Leja, J., Conroy, C., & Speagle, J. S. 2021, *ApJS*, 254, 22, doi: [10.3847/1538-4365/abef67](https://doi.org/10.3847/1538-4365/abef67)
- Kasen, D., Thomas, R. C., & Nugent, P. 2006, *ApJ*, 651, 366, doi: [10.1086/506190](https://doi.org/10.1086/506190)
- Kasliwal, M. M., Kulkarni, S. R., Gal-Yam, A., et al. 2012, *ApJ*, 755, 161, doi: [10.1088/0004-637X/755/2/161](https://doi.org/10.1088/0004-637X/755/2/161)
- Kasliwal, M. M., Cannella, C., Bagdasaryan, A., et al. 2019, *PASP*, 131, 038003, doi: [10.1088/1538-3873/aafbc2](https://doi.org/10.1088/1538-3873/aafbc2)
- Kauffmann, G., Heckman, T. M., White, S. D. M., et al. 2003, *MNRAS*, 341, 33, doi: [10.1046/j.1365-8711.2003.06291.x](https://doi.org/10.1046/j.1365-8711.2003.06291.x)
- Kromer, M., Sim, S. A., Fink, M., et al. 2010, *ApJ*, 719, 1067, doi: [10.1088/0004-637X/719/2/1067](https://doi.org/10.1088/0004-637X/719/2/1067)
- Kupfer, T., Bauer, E. B., van Roestel, J., et al. 2022, *ApJL*, 925, L12, doi: [10.3847/2041-8213/ac48f1](https://doi.org/10.3847/2041-8213/ac48f1)
- Lang, D. 2014, *AJ*, 147, 108, doi: [10.1088/0004-6256/147/5/108](https://doi.org/10.1088/0004-6256/147/5/108)
- Leroy, A. K., Sandstrom, K. M., Lang, D., et al. 2019, *ApJS*, 244, 24, doi: [10.3847/1538-4365/ab3925](https://doi.org/10.3847/1538-4365/ab3925)
- Livne, E. 1990, *ApJL*, 354, L53, doi: [10.1086/185721](https://doi.org/10.1086/185721)
- Livne, E., & Arnett, D. 1995, *ApJ*, 452, 62, doi: [10.1086/176279](https://doi.org/10.1086/176279)
- Lucy, L. B. 1991, *ApJ*, 383, 308, doi: [10.1086/170787](https://doi.org/10.1086/170787)
- Lunnan, R., Kasliwal, M. M., Cao, Y., et al. 2017, *ApJ*, 836, 60, doi: [10.3847/1538-4357/836/1/60](https://doi.org/10.3847/1538-4357/836/1/60)
- Lyman, J. D., Levan, A. J., Church, R. P., Davies, M. B., & Tanvir, N. R. 2014, *MNRAS*, 444, 2157, doi: [10.1093/mnras/stu1574](https://doi.org/10.1093/mnras/stu1574)
- Magee, M. R., Maguire, K., Kotak, R., & Sim, S. A. 2021, *MNRAS*, 502, 3533, doi: [10.1093/mnras/stab201](https://doi.org/10.1093/mnras/stab201)
- Maguire, K., Sullivan, M., Pan, Y. C., et al. 2014, *MNRAS*, 444, 3258, doi: [10.1093/mnras/stu1607](https://doi.org/10.1093/mnras/stu1607)
- Mahabal, A., Rebbapragada, U., Walters, R., et al. 2019, *PASP*, 131, 038002, doi: [10.1088/1538-3873/aaf3fa](https://doi.org/10.1088/1538-3873/aaf3fa)
- Mainzer, A., Bauer, J., Cutri, R. M., et al. 2014, *ApJ*, 792, 30, doi: [10.1088/0004-637X/792/1/30](https://doi.org/10.1088/0004-637X/792/1/30)
- Maoz, D., Mannucci, F., & Nelemans, G. 2014, *ARA&A*, 52, 107, doi: [10.1146/annurev-astro-082812-141031](https://doi.org/10.1146/annurev-astro-082812-141031)
- Marion, G. H., Höflich, P., Gerardy, C. L., et al. 2009, *AJ*, 138, 727, doi: [10.1088/0004-6256/138/3/727](https://doi.org/10.1088/0004-6256/138/3/727)
- Martin, D. C., Fanson, J., Schiminovich, D., et al. 2005, *ApJL*, 619, L1, doi: [10.1086/426387](https://doi.org/10.1086/426387)
- Masci, F. J., Laher, R. R., Rusholme, B., et al. 2019, *PASP*, 131, 018003, doi: [10.1088/1538-3873/aae8ac](https://doi.org/10.1088/1538-3873/aae8ac)
- Matheson, T., Filippenko, A. V., Barth, A. J., et al. 2000, *AJ*, 120, 1487, doi: [10.1086/301518](https://doi.org/10.1086/301518)
- Mazzali, P. A., Benetti, S., Altavilla, G., et al. 2005, *ApJL*, 623, L37, doi: [10.1086/429874](https://doi.org/10.1086/429874)
- Mazzali, P. A., Sullivan, M., Hachinger, S., et al. 2014, *MNRAS*, 439, 1959, doi: [10.1093/mnras/stu077](https://doi.org/10.1093/mnras/stu077)
- Mazzali, P. A., Sullivan, M., Filippenko, A. V., et al. 2015, *MNRAS*, 450, 2631, doi: [10.1093/mnras/stv761](https://doi.org/10.1093/mnras/stv761)
- McMahon, R. G., Banerji, M., Gonzalez, E., et al. 2013, *The Messenger*, 154, 35
- Meisner, A. M., Lang, D., & Schlegel, D. J. 2017, *AJ*, 153, 38, doi: [10.3847/1538-3881/153/1/38](https://doi.org/10.3847/1538-3881/153/1/38)
- . 2018, *Research Notes of the American Astronomical Society*, 2, 1, doi: [10.3847/2515-5172/aaa4bc](https://doi.org/10.3847/2515-5172/aaa4bc)

- Miller, J., & Stone, R. 1994, The Kast Double Spectrograph, Lick Observatory technical reports (University of California Observatories/Lick Observatory).
<https://books.google.com/books?id=QXk2AQAAIAAJ>
- Ni, Y. Q., Moon, D.-S., Drout, M. R., et al. 2022a, *Nature Astronomy*, doi: [10.1038/s41550-022-01603-4](https://doi.org/10.1038/s41550-022-01603-4)
- . 2022b, arXiv e-prints, arXiv:2206.12437.
<https://arxiv.org/abs/2206.12437>
- Nomoto, K. 1982a, *ApJ*, 253, 798, doi: [10.1086/159682](https://doi.org/10.1086/159682)
- . 1982b, *ApJ*, 257, 780, doi: [10.1086/160031](https://doi.org/10.1086/160031)
- Nugent, A. E., Fong, W., Dong, Y., et al. 2020, *ApJ*, 904, 52, doi: [10.3847/1538-4357/abc24a](https://doi.org/10.3847/1538-4357/abc24a)
- . 2022, arXiv e-prints, arXiv:2206.01764.
<https://arxiv.org/abs/2206.01764>
- Oke, J. B., & Gunn, J. E. 1982, *PASP*, 94, 586, doi: [10.1086/131027](https://doi.org/10.1086/131027)
- Oke, J. B., Cohen, J. G., Carr, M., et al. 1995, *PASP*, 107, 375, doi: [10.1086/133562](https://doi.org/10.1086/133562)
- Osterbrock, D. E., & Ferland, G. J. 2006, *Astrophysics of gaseous nebulae and active galactic nuclei*
- Patterson, M. T., Bellm, E. C., Rusholme, B., et al. 2019, *PASP*, 131, 018001, doi: [10.1088/1538-3873/aae904](https://doi.org/10.1088/1538-3873/aae904)
- Pereira, R., Thomas, R. C., Aldering, G., et al. 2013, *A&A*, 554, A27, doi: [10.1051/0004-6361/201221008](https://doi.org/10.1051/0004-6361/201221008)
- Perets, H. B., Gal-Yam, A., Mazzali, P. A., et al. 2010, *Nature*, 465, 322, doi: [10.1038/nature09056](https://doi.org/10.1038/nature09056)
- Polin, A., Nugent, P., & Kasen, D. 2019, *ApJ*, 873, 84, doi: [10.3847/1538-4357/aafb6a](https://doi.org/10.3847/1538-4357/aafb6a)
- . 2021, *ApJ*, 906, 65, doi: [10.3847/1538-4357/abcccc](https://doi.org/10.3847/1538-4357/abcccc)
- Poznanski, D., Ganeshalingam, M., Silverman, J. M., & Filippenko, A. V. 2011, *MNRAS*, 415, L81, doi: [10.1111/j.1745-3933.2011.01084.x](https://doi.org/10.1111/j.1745-3933.2011.01084.x)
- Prochaska, J. X., Hennawi, J. F., Westfall, K. B., et al. 2020, *Journal of Open Source Software*, 5, 2308, doi: [10.21105/joss.02308](https://doi.org/10.21105/joss.02308)
- Prochaska, J. X., Hennawi, J., Cooke, R., et al. 2020, *pypeit/PypeIt: Release 1.0.0, v1.0.0*, Zenodo, doi: [10.5281/zenodo.3743493](https://doi.org/10.5281/zenodo.3743493)
- Rigault, M., Neill, J. D., Blagorodnova, N., et al. 2019, *A&A*, 627, A115, doi: [10.1051/0004-6361/201935344](https://doi.org/10.1051/0004-6361/201935344)
- Sanders, J. L., Belokurov, V., & Man, K. T. F. 2021, *MNRAS*, 506, 4321, doi: [10.1093/mnras/stab1951](https://doi.org/10.1093/mnras/stab1951)
- Schlaflly, E. F., & Finkbeiner, D. P. 2011, *ApJ*, 737, 103, doi: [10.1088/0004-637X/737/2/103](https://doi.org/10.1088/0004-637X/737/2/103)
- Schulze, S., Yaron, O., Sollerman, J., et al. 2021, *ApJS*, 255, 29, doi: [10.3847/1538-4365/abff5e](https://doi.org/10.3847/1538-4365/abff5e)
- Shahbandeh, M., Hsiao, E. Y., Ashall, C., et al. 2022, *ApJ*, 925, 175, doi: [10.3847/1538-4357/ac4030](https://doi.org/10.3847/1538-4357/ac4030)
- Shen, K. J., Boos, S. J., Townsley, D. M., & Kasen, D. 2021, *ApJ*, 922, 68, doi: [10.3847/1538-4357/ac2304](https://doi.org/10.3847/1538-4357/ac2304)
- Shen, K. J., & Moore, K. 2014, *ApJ*, 797, 46, doi: [10.1088/0004-637X/797/1/46](https://doi.org/10.1088/0004-637X/797/1/46)
- Shen, K. J., Quataert, E., & Pakmor, R. 2019, *ApJ*, 887, 180, doi: [10.3847/1538-4357/ab5370](https://doi.org/10.3847/1538-4357/ab5370)
- Silverman, J. M., Vinkó, J., Marion, G. H., et al. 2015, *MNRAS*, 451, 1973, doi: [10.1093/mnras/stv1011](https://doi.org/10.1093/mnras/stv1011)
- Silverman, J. M., Foley, R. J., Filippenko, A. V., et al. 2012, *MNRAS*, 425, 1789, doi: [10.1111/j.1365-2966.2012.21270.x](https://doi.org/10.1111/j.1365-2966.2012.21270.x)
- Sim, S. A., Fink, M., Kromer, M., et al. 2012, *MNRAS*, 420, 3003, doi: [10.1111/j.1365-2966.2011.20162.x](https://doi.org/10.1111/j.1365-2966.2011.20162.x)
- Skrutskie, M. F., Cutri, R. M., Stiening, R., et al. 2006, *AJ*, 131, 1163, doi: [10.1086/498708](https://doi.org/10.1086/498708)
- Smith, M., Nichol, R. C., Dilday, B., et al. 2012, *ApJ*, 755, 61, doi: [10.1088/0004-637X/755/1/61](https://doi.org/10.1088/0004-637X/755/1/61)
- Speagle, J. S. 2020, *MNRAS*, 493, 3132, doi: [10.1093/mnras/staa278](https://doi.org/10.1093/mnras/staa278)
- Sullivan, M., Le Borgne, D., Pritchett, C. J., et al. 2006, *ApJ*, 648, 868, doi: [10.1086/506137](https://doi.org/10.1086/506137)
- Sullivan, M., Kasliwal, M. M., Nugent, P. E., et al. 2011, *ApJ*, 732, 118, doi: [10.1088/0004-637X/732/2/118](https://doi.org/10.1088/0004-637X/732/2/118)
- Sun, F., & Gal-Yam, A. 2017, arXiv e-prints, arXiv:1707.02543. <https://arxiv.org/abs/1707.02543>
- Townsley, D. M., Miles, B. J., Shen, K. J., & Kasen, D. 2019, *ApJL*, 878, L38, doi: [10.3847/2041-8213/ab27cd](https://doi.org/10.3847/2041-8213/ab27cd)
- Valenti, S., Yuan, F., Taubenberger, S., et al. 2014, *MNRAS*, 437, 1519, doi: [10.1093/mnras/stt1983](https://doi.org/10.1093/mnras/stt1983)
- Veilleux, S., & Osterbrock, D. E. 1987, *ApJS*, 63, 295, doi: [10.1086/191166](https://doi.org/10.1086/191166)
- Virtanen, P., Gommers, R., Oliphant, T. E., et al. 2020, *Nature Methods*, 17, 261, doi: [10.1038/s41592-019-0686-2](https://doi.org/10.1038/s41592-019-0686-2)
- Waskom, M. L. 2021, *Journal of Open Source Software*, 6, 3021, doi: [10.21105/joss.03021](https://doi.org/10.21105/joss.03021)
- Woosley, S. E., & Kasen, D. 2011, *ApJ*, 734, 38, doi: [10.1088/0004-637X/734/1/38](https://doi.org/10.1088/0004-637X/734/1/38)
- Woosley, S. E., Taam, R. E., & Weaver, T. A. 1986, *ApJ*, 301, 601, doi: [10.1086/163926](https://doi.org/10.1086/163926)
- Woosley, S. E., & Weaver, T. A. 1994, *ApJ*, 423, 371, doi: [10.1086/173813](https://doi.org/10.1086/173813)
- Wright, A. H. 2016, *LAMBDA: Lambda Adaptive Multi-Band Deblending Algorithm in R*, *Astrophysics Source Code Library*, record ascl:1604.003. <http://ascl.net/1604.003>
- Wright, E. L., Eisenhardt, P. R. M., Mainzer, A. K., et al. 2010, *AJ*, 140, 1868, doi: [10.1088/0004-6256/140/6/1868](https://doi.org/10.1088/0004-6256/140/6/1868)
- Yao, Y., Miller, A. A., Kulkarni, S. R., et al. 2019, *ApJ*, 886, 152, doi: [10.3847/1538-4357/ab4cf5](https://doi.org/10.3847/1538-4357/ab4cf5)
- Yaron, O., & Gal-Yam, A. 2012, *PASP*, 124, 668, doi: [10.1086/666656](https://doi.org/10.1086/666656)

York, D. G., Adelman, J., Anderson, John E., J., et al.
2000, AJ, 120, 1579, doi: [10.1086/301513](https://doi.org/10.1086/301513)

Zackay, B., Ofek, E. O., & Gal-Yam, A. 2016, ApJ, 830, 27,
doi: [10.3847/0004-637X/830/1/27](https://doi.org/10.3847/0004-637X/830/1/27)